

POLITECNICO DI TORINO

---

Department of Mechanical and Aerospace Engineering

Master degree course in Aerospace Engineering

Master Degree Thesis

**Development and Validation  
of Algorithms for Vibration Monitoring  
of Aeronautical Engines**



**Supervisors**

Prof. Paolo Maggiore  
Ing. Marco Moletta

**Candidate**

Alberto CIVARDI  
Student number: 252406

---

ACADEMIC YEAR 2019-2020



## **Abstract**

The main concern of the aeronautical industry has been to increase engine efficiency in the last decades. This parameter is strictly related to the dynamic properties of blades and disk constituting modern multi-stage turbofan. As a consequence, the design of blades and disks is focused on weight reduction, giving room for the enhancing of mechanical vibrations. In such a context robust computational techniques and innovative measurement systems have become necessary tools to guarantee structural integrity of the engine. Furthermore, new testing methods have been introduced, as the one described in the main part of the thesis, in which a magnetic forcing in vacuum is applied to the reference test article.

The topics developed in this thesis work concern the study of experimental data of Ge Avio's multi-stage bladed disks, starting from the development of algorithms to clean data and the creation of a GUI (Graphic User Interface) following a benchmarking activity. These tools were then applied to the aforementioned testing activity, both to traditional acquisition methods for vibration measurements, Strain Gauges (SGs), and to a more innovative method the blade tip timing (BTT). As a matter of fact, the influence of magnetic field on SGs measurements is not negligible, causing the rise of a disturbance proportional with rotational speed of the test article. Therefore, if on the one hand, algorithms to eliminate this linear offset were applied in order to correctly estimate Q factor and vibration amplitude of certain blades starting from SGs data, on the other hand, a laser based method was introduced (BTT), since it is not subject to magnetic disturbance by definition, and a comparison between the two methods is suggested.

# Contents

<b>List of Figures</b>	III
<b>1 Introduction</b>	1
1.1 The GREAT 2020 . . . . .	1
<b>2 Aeronautical Engines</b>	4
2.1 Main Architectures . . . . .	4
2.1.1 Turbojet . . . . .	5
2.1.2 Turbofan . . . . .	5
2.1.3 Turboprop . . . . .	7
2.1.4 Turboshaft . . . . .	8
2.2 Low-Pressure Turbine (LPT) . . . . .	9
2.2.1 Blading Architecture . . . . .	10
<b>3 Rotordynamics</b>	13
3.1 Static Analysis . . . . .	13
3.2 Dynamic Analysis . . . . .	14
3.2.1 Aeroelasticity . . . . .	15
3.2.2 Free Vibration Analysis . . . . .	16
3.2.3 Forced Response . . . . .	18
3.2.4 Flutter . . . . .	21
3.3 Cyclic Symmetry . . . . .	23
3.4 Modal Analysis . . . . .	27
3.4.1 Modeshapes . . . . .	30
3.4.2 FreND Diagram . . . . .	32
<b>4 Introduction to Signal Analysis</b>	34
4.1 Signal Classification . . . . .	34
4.1.1 Fourier Transform . . . . .	35

4.2	Signal Preprocessing . . . . .	39
4.2.1	Sampling . . . . .	39
4.2.2	Truncation and Windowing . . . . .	43
4.2.3	Frequency discretization . . . . .	48
<b>5</b>	<b>Code Architecture</b>	<b>52</b>
5.1	Code Input . . . . .	53
5.2	Code Output . . . . .	55
<b>6</b>	<b>Tool Applications</b>	<b>62</b>
6.1	The Spinning Test Rig . . . . .	62
6.1.1	The Dummy Disks . . . . .	63
6.1.2	The Excitation System . . . . .	64
6.2	The Strain Measurement System . . . . .	66
6.2.1	Strain Gauges Postprocessing . . . . .	68
6.3	The Blade Tip-Timing Measurement System . . . . .	79
6.3.1	The Beam Shutter Method and the Sensor Positioning . . . . .	81
6.4	BTT Postprocessing . . . . .	83
<b>7</b>	<b>Conclusions</b>	<b>90</b>
	<b>Bibliography</b>	<b>90</b>

# List of Figures

1.1	ACARE objectives . . . . .	2
2.1	Jet engine and its main components [16] . . . . .	5
2.2	Turbojet architecture . . . . .	6
2.3	Turbojet scheme . . . . .	6
2.4	Turbofan architecture . . . . .	7
2.5	Turbofan scheme . . . . .	7
2.6	Turboprop architecture . . . . .	8
2.7	Turboshaft architecture . . . . .	8
2.8	Turbine cross-section [15] . . . . .	9
2.9	General blade and vane configurations [11] . . . . .	12
3.1	Interaction between disciplines [19] . . . . .	15
3.2	Excited blading stage . . . . .	16
3.3	Example of bending (left) and torsional (right) modes . . . . .	18
3.4	Variable change in order to pass from a fixed to a rotating system . . . . .	19
3.5	Forward and backward forces [16] . . . . .	20
3.6	Campbell diagram [10] . . . . .	21
3.7	Flutter oscillation . . . . .	22
3.8	Cyclic symmetry . . . . .	25
3.9	Cyclic symmetry conditions . . . . .	26
3.10	DOF division in the $n$ th-sector . . . . .	28
3.11	Bladed disk vibration modes at vary nodal diameters (ND) and nodal circumferences (NC) [4] . . . . .	30
3.12	Standing wave . . . . .	31
3.13	Stationary mode [6] . . . . .	31
3.14	Rotating wave . . . . .	31
3.15	Rotating mode [6] . . . . .	32
3.16	FreND diagram [8] . . . . .	33
4.1	Stationary signals division . . . . .	35

4.2	Time domain and Frequency domain . . . . .	36
4.3	Sine waves composing the signal with frequencies of 20 and 60 Hz [7] . . .	37
4.4	Sine waves composing the signal with frequencies of 20 and 60 Hz [7] . . .	37
4.5	Signal with random noise added [7] . . . . .	38
4.6	Spectrum of the signal $S(t)$ [7] . . . . .	38
4.7	Generic signal with a limited bandwidth . . . . .	40
4.8	Pulse train in time domain . . . . .	40
4.9	Pulse train in frequency domain . . . . .	40
4.10	Sampled signal in time domain . . . . .	41
4.11	Signal spectrum which does not respect Nyquist condition . . . . .	42
4.12	Sampling frequency impulses . . . . .	42
4.13	Anti-aliasing filter . . . . .	43
4.14	Aliasing effect . . . . .	43
4.15	Windowing functions [7] . . . . .	45
4.16	Windowed 5 Hz sine signal and its spectrum with $\Delta f = 2/3Hz$ [7] . . . .	46
4.17	Windowed 4 Hz sine signal and its spectrum with $\Delta f = 2/3Hz$ [7] . . . .	46
4.18	Overlapped signal [7] . . . . .	47
4.19	Visual representation of the picket fence effect [7] . . . . .	48
4.20	Picket fence effect errors of different windows [7] . . . . .	49
4.21	Picket fence effect errors of different windows [7] . . . . .	50
5.1	Frequency analysis workflow [7] . . . . .	52
5.2	Velocity ramp selection . . . . .	54
5.3	Colormap with x-axis rotational speed [7] . . . . .	56
5.4	Peak isolated with the Peak snap function and its detrended signal . . . .	57
5.5	In green the original unevenly spaced x-axis vector, in blue the new evenly spaced one. In red the error introduced by this procedure . . . . .	59
5.6	Frequency resolution variable along y-axis . . . . .	60
6.1	The spinning rig a) and the supporting rings for the magnets and laser sensors positioning b) [3] . . . . .	63
6.2	The dummy disk 1 within the spinning test rig [3] . . . . .	63
6.3	The dummy disk 2 within the spinning test rig [3] . . . . .	64
6.4	Fixed magnet and load cell exciting the rotating disk [3] . . . . .	65
6.5	Magnetic force profile acting on each blade a) and its harmonic content b). . . . .	66
6.6	Strain gauge . . . . .	67
6.7	Strain gauge at the blade root of the dummy disk 1 a), strain gauge at the back of the airfoil of a dummy disk 2 blade b) [3] . . . . .	67
6.8	FreND diagram for the dummy disk 2 [3] . . . . .	68

6.9	Magnetic disturbance resulting in a linear offset . . . . .	69
6.10	Q factor parameters . . . . .	70
6.11	De-trending result . . . . .	71
6.12	Color code assigned to signal quality . . . . .	74
6.13	Data selected . . . . .	75
6.14	De-trending options . . . . .	75
6.15	BTT measurement system [18] . . . . .	80
6.16	ToA variation [18] . . . . .	81
6.17	Beam shutter configuration for the dummy disk 1 [3] . . . . .	82
6.18	Beam shutter configuration for the dummy disk 2 [3] . . . . .	82
6.19	Angular sensors' position . . . . .	84
6.20	Velocity profile . . . . .	84
6.21	Inter-Blade Distance evaluation . . . . .	85
6.22	FFT result . . . . .	85
6.23	Peak shape evaluation for each vibrating blade . . . . .	86
6.24	SG04 frequency spectrum . . . . .	87
6.25	Blade 52 frequency spectrum . . . . .	87
6.26	SG04 vs Blade 52 frequency spectrum . . . . .	88
6.27	SG method vs BTT . . . . .	89

# Chapter 1

## Introduction

### 1.1 The GREAT 2020

The thesis work developed in these months is intended as part of the GREAT2020 project (Green Engine for Air Traffic). The project started in 2009 when the European Commission, along with many experts of the Advisory Council for Aviation Research and Innovation in Europe (ACARE), became aware of the need to set new targets to the expanding aeronautical industry to be reached within 2020, to reduce its environmental impact.

Among the aeronautical companies involved, the main actors of the GREAT 2020 are:

- **AvioAero:** a GE Aviation business, leader in the design, maintenance and manufacturing of aeronautical components, which constitutes a centre of competence for the entire General Electric group regarding mechanical transmissions and low-pressure turbine design, with locations in Turin, Pomigliano D'Arco and Poland.
- **Politecnico di Torino:** one of the most prestigious public organizations worldwide for its formation and research activities in engineering and architecture. A prime actor of the project is the Greatlab, a shared working area born in 2008 from the partnership between Politecnico di Torino and AvioAero.
- **ISTEC-CNR:** The Turin detail of the Istituto di Scienza e Tecnologia dei materiali Ceramici which as part of the GREAT2020 researches environmentally-friendly processing systems of aeronautical alloys.
- **La Regione Piemonte:** host of the project and ideal soil for the development and the growth of the GREAT 2020, who has always been committed to the promotion of

industrial competitiveness, resulting in active support for the GREAT2020 project.

The GREAT2020 project has the ambitious goal of reducing chemical emissions generated by the combustion process of an aeronautical engine within 2020. More in-depth, the objective is to dramatically decrease the emissions of  $CO_2$ , by 50%, of  $NO_x$ , by 80%, and to decrease the perceived noise by 10dB to the technologies of 2000s, as shown in figure 1.1 below.

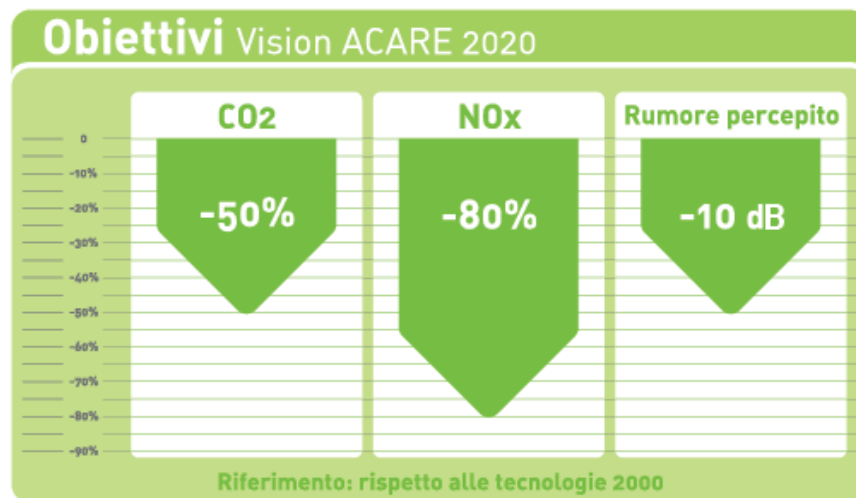


Figure 1.1: ACARE objectives

On the one hand, to reduce carbon dioxide emissions, important modifications in the quantity of fuel burned by aeronautical engines are required, which requires either an increase of the total efficiency or a reduction of its weight. Avio Aero is currently investing a lot of resources towards the least objective, focusing its efforts on Additive Manufacturing. This innovative production process allows producing complex geometries (such as hollow blades) by successively adding material layer by layer, resulting in a money and mass saving.

On the other hand,  $NO_x$  emissions are not only proportional to the fuel burned but also to the thermal conditions of the combustion chamber; which means that an increase in the thermal efficiency of the engine could have the side effect of rising nitrogen oxide emissions. Therefore the development of specific combustion technologies is required, and among the many, the most promising is the "Lean-Burn", which reduced the peak temperature of the engine by guaranteeing a high air-to-fuel ratio near the flame.

Such ambitious goals are not necessary since the environmental impact of air traffic is pronounced now, which is just the 4,6% of the total effect of humanity on climate, but

for what the emissions will be in 20 years when the global fleet is expected to double.

## Chapter 2

# Aeronautical Engines

In this chapter, main propulsion architectures are described, in order to completely understand and contextualize this thesis work. Considering the complexity of the argument, the exposed concepts are intended to give just a general introduction to the matter in order to acquire sufficient knowledge of aeronautical engines.

### 2.1 Main Architectures

The aeronautical sector is constantly changing due to very variable market demands which require different types of aircraft. Mission profiles can be of various types, spanning from passenger or goods transport to surveillance, rescue and military missions. By consequence, there are various engine architectures to optimally satisfy the requirements of each condition.

The third Newton law is the basic to generate thrust, also known as the action-reaction principle which says: "For every action, there is an equal and opposite reaction". Concerning jet engines, an external air mass is accelerated inside a duct to produce the thrust as a reaction. The main components which constitute the jet engine are:

- Air intake: Interface between external and internal environment, in order to control the incoming air mass, and to correct its direction and velocity to optimize subsequent phases.
- Compressor: It's usually divided into Low-Pressure Compressor (LPC), and High-Pressure Compressor (HPC) and ideally covers the role to compress the incoming flux isotropically.
- Combustion chamber: It mixes air flux and fuel with a ratio of 50:1 and activates the combustion considering as limit temperature the maximum for the material.

- Turbine: It is usually divided into the High-Pressure Turbine (HPT) and the Low-Pressure Turbine (LPT), which expands the flux in order to produce the necessary power for the compressor.
- Exhaust nozzle: It accelerates and terminates the expansion of the exhaust gases obtaining thrust.

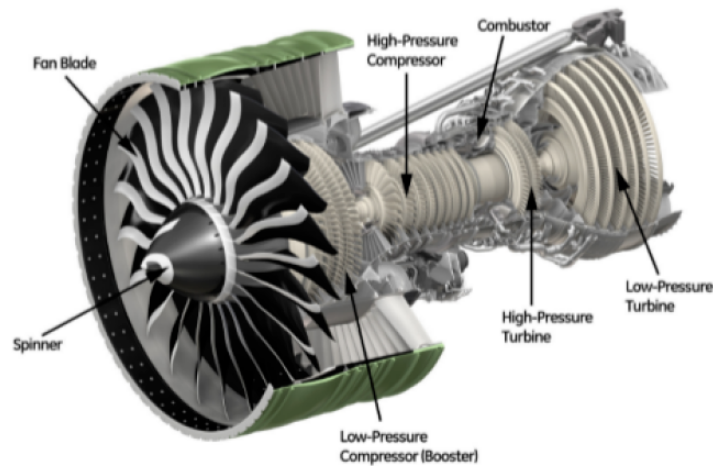


Figure 2.1: Jet engine and its main components [16]

### 2.1.1 Turbojet

This type of air-breathing engine is no longer used but has to be considered an ancestor of modern aeronautical engines: turbofan, turboprop and turboshaft. Compared to previous architectures, the turbojet shows better performance thanks to the thrust obtained by compressing, igniting and expanding the flux. More in-depth thrust is obtained thanks to the high difference between the momentum of air incoming through the intake and the one outgoing through the nozzle. The power generated by the turbine is transmitted to the compressor thanks to a connecting shaft (fig. 2.2, 2.3).

### 2.1.2 Turbofan

The turbofan is the logical evolution of the turbojet designed to enhance efficiency and performance by introducing an extra fan at the beginning of the engine. The air mass, once passed through a ducted fan it's divided into two fluxes:

- Hot flux which follows all the phases of the turbojet cycle

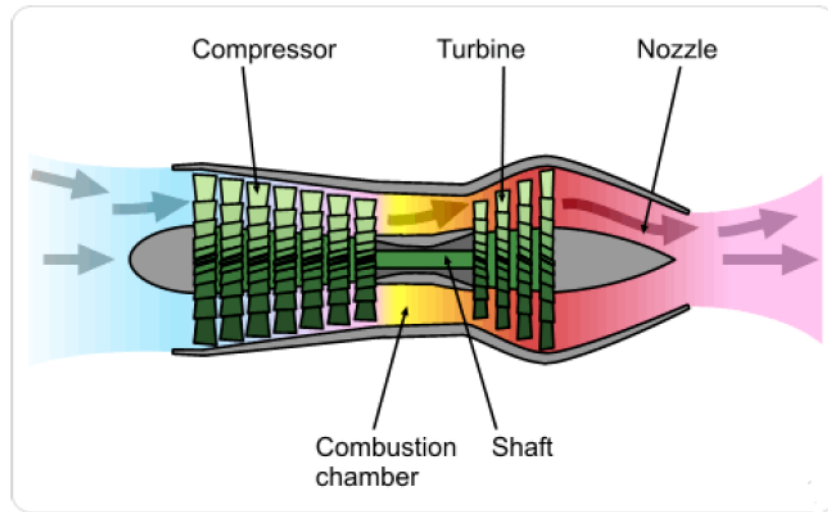


Figure 2.2: Turbojet architecture

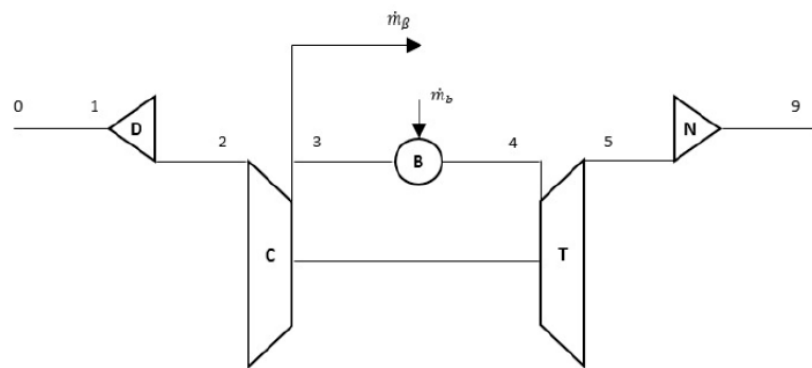


Figure 2.3: Turbojet scheme

- Cold flux which is led towards another nozzle.

This configuration is highly convenient in terms of thrust generation and fuel consumption, considering the propulsion efficiency. The difference with the previous approach consists of the principle for which the same thrust can be obtained through a low acceleration of a large air mass rather than a great acceleration of a limited air mass. Furthermore, thanks to the mixing generated between the by-passed air and the exhaust gases, a consistent reduction of noise pollution is obtained (fig 2.4, 2.5).



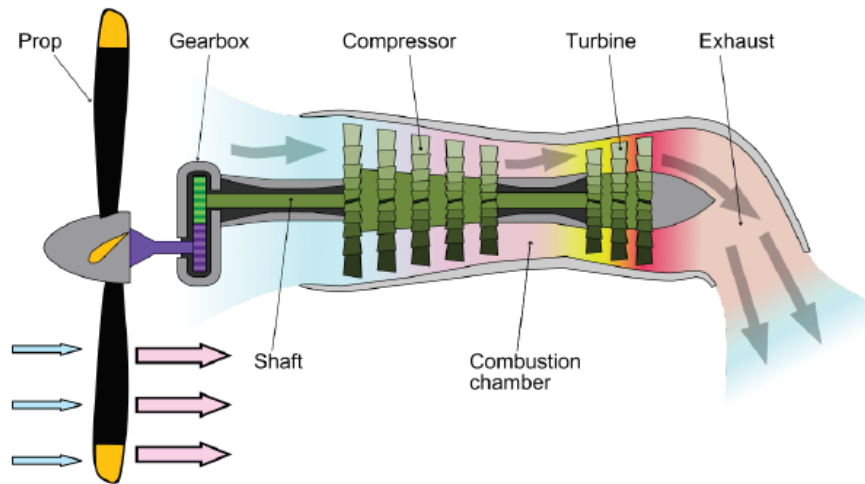


Figure 2.6: Turboprop architecture

#### 2.1.4 Turboshaft

The turboshaft is a variation of the turbojet with additional turbine expansion to extract heat energy from the exhaust and convert it into output shaft power. Turboshaft engines are commonly used in an application that requires a sustained high power output, high reliability, small size and lightweight (helicopters (fig. 2.7)).

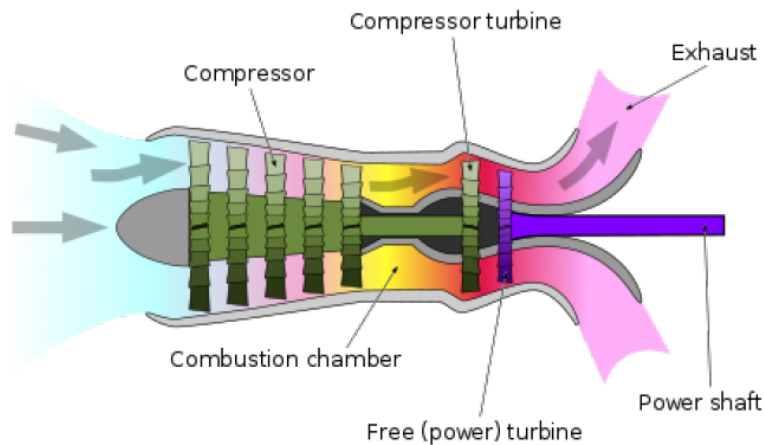


Figure 2.7: Turboshaft architecture

## 2.2 Low-Pressure Turbine (LPT)

The objective of this section is to introduce the basics of this engine component in order to have a general insight useful to understand the post-processing activity that follows. Turbines can be classified as axial, radial or mixed machines, depending on their usage. More in-depth, the axial machine is meant to process higher air flows with respect to the radial configuration, but in the case of lower fluxes, the efficiency decrease and greater stage pressure ratios. In air-breathing engines, axial turbines are employed with greater efficiency with respect to compressor ones because it is less probable that flux separation occurs during expansion than compression. During the design phase, it is of prime importance to take under consideration thermo-mechanical and fluid dynamical stress. In order to enhance the efficiency, the expansion work is divided into several stages composed of a succession of rotors and stators in order to minimize the fluid dynamical counter-effects. The typical two-shaft configuration consists of a first hollow shaft, which connects and transmit power from the High-Pressure Turbine (HPT) to the High-Pressure Compressor (HPC), and of another inner shaft, which interconnects the Low-Pressure Turbine (LPT) (fig. 2.8) and the Low-Pressure Compressor (LPC). As a consequence, a careful analysis of the physical behaviour of the LPT is fundamental in order to foresee its mode of operation in critical conditions and to maximize its efficiency.

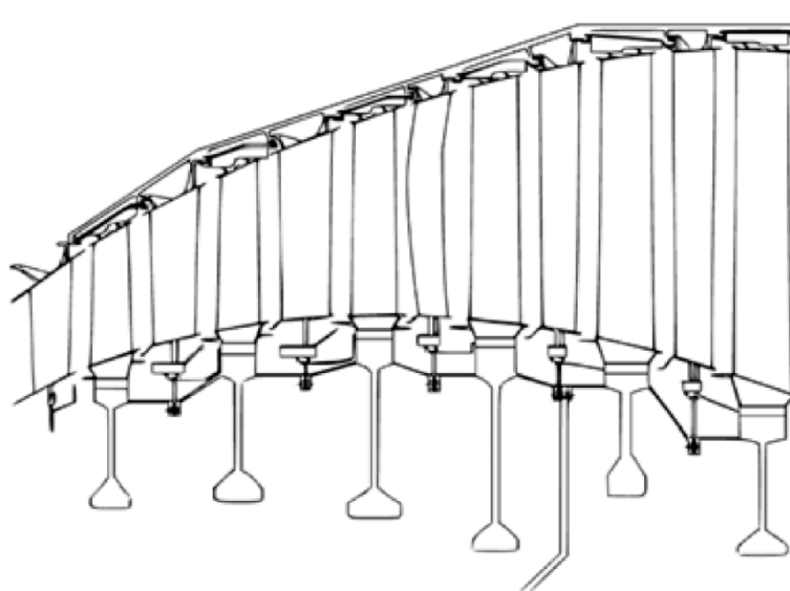


Figure 2.8: Turbine cross-section [15]

### 2.2.1 Blading Architecture

The turbine generates work thanks to blades rotation induced by the exhaust gases flux. Therefore its structure needs optimization to guarantee maximum performance, taking under consideration mechanical, thermal, aerodynamic, pressure and fatigue loads. The turbine architecture, particularly so, is composed of a rotating disk connected to blades with optimized airfoils.

In order to obtain the desired expansion ratio, a 1D aerodynamic design of the guide vane and turbine is performed, aiming to obtain a disposition which guarantees the desired efficiency and mechanical power output.

Therefore, starting from the velocity triangles and the well-known turbo-machinery equations, it is possible to correctly predict the mechanical power extracted by the turbine 2.1, in the case of an axial turbine.

$$P = \dot{m} \cdot (u_1 c_{1u} - u_2 c_{2u}) \quad (2.1)$$

Where  $\dot{m}$  represents the mass flow rate,  $u$  is the rotor blade speed, and  $c_u$  is the tangential speed of the fluid, which is the projection of the absolute velocity along the  $u$  direction. The subscripts 1 and 2 refer respectively to the inlet and outlet of the rotor blade. Since in an axial turbo-machine all the points of the blade have the same angular speed at the same radius, in this case,  $u_1 = u_2$ .

Another important parameter to take under consideration in the design phase of a turbine is the degree of reaction 2.2, which is a non-dimensional parameter that describes the behaviour of a turbine, by representing how the expansion phase is split between rotor and stator.

$$R = \frac{\Delta H_{rotor}}{\Delta H_{total}} = \frac{h_2 - h_1}{h_{01} - h_{03}} \quad (2.2)$$

The degree of reaction is clearly equals to zero in an impulse turbine, and to one in a reaction one. Usually in aeronautical applications impulse-reaction turbine are employed, with  $R = 0.5$ .

Consider now the design of each component starting from the disk where it is necessary to consider the inertial loads generated, caused by its high rotational velocity, and the external loads transmitted through blades fixing. The thermal load can be overlooked since the disk is thermally isolated from the flux through a holding. In the blade design instead, either thermal or inertial loads have to be taken under consideration besides the loads generated by the interaction with the flux. As a consequence, the blade material is exposed to high temperatures and centrifugal forces, which complicate its structural

resistance. This is even more complex, taking into account that an optimal airfoil requires a thin profile.

As regarding the 3D design of the blade, their shape is usually "twisted", by increasing the angle with the radial distance. This configuration is important to counter-balance the fact that at high radius, the fluid is more subject to centrifugal force. This twisted configuration creates a pressure field which forces the fluid downwards.

The entire design activity is based on the free vortex theory, which causes the degree of reaction to change continuously from root to tip. Another important characteristic is that the stagger angle is kept variable with the radius to obtain a constant relative velocity and, as a consequence, work.

The design activity obviously differs between stators and rotors. The former has an airfoil which is clamped at its end, where there are the Outer Band Vane (OBV) and the Inner Band Vane (IBV). The latter, instead, consists of the following elements:

- Shroud: a component positioned over the blade which ensures tightness, in order to limit pressure losses, and increases its overall stiffness thanks to the blade to blade connection called interlocking.
- Airfoil: central part of the blade with an optimized airfoil which directly interacts with the flux to generate same work and uniform axial velocity in the radial direction.
- Shank: connecting element between the airfoil and the part fixed to the disk
- Dovetail: optimal coupling element between blade and disk which resists to all generated loads.

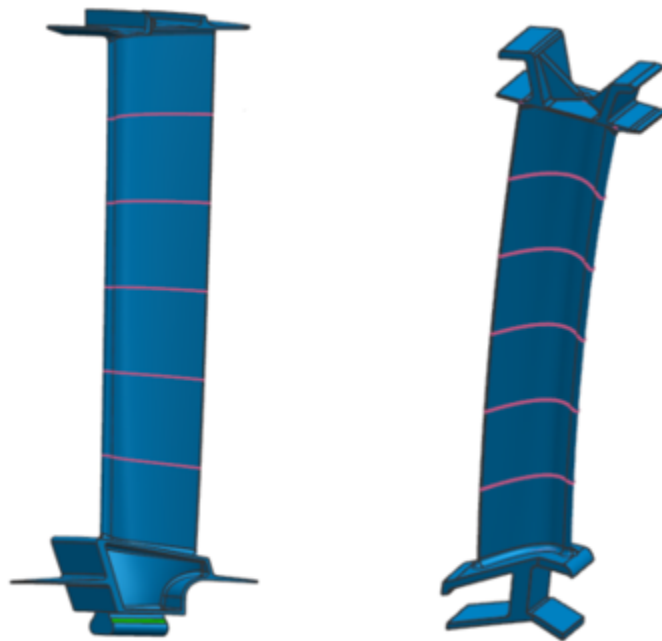


Figure 2.9: General blade and vane configurations [11]

## Chapter 3

# Rotordynamics

In the design phase of a Low-Pressure Turbine, it is fundamental to accurately analyze the common vibrating patterns that originate during the operational phase.

First of all, it is important to give a classification of the main loads (inertial, thermal and aerodynamic) based on their evolution in time:

- Static loads: Constant forces or subjected to a limited variation in time
- Quasi-static loading: Forces originated by dynamic phenomena but with constant temporal characteristics.
- Dynamic loads: Forces variable in time that presents very high gradients which cause not negligible dynamic effects.

The main characteristic to distinguish a static load from a dynamic one is the frequency at which occurs, indeed if it is far below the minimum natural frequency of the structure, the load is identified as static or quasi-static. By contrast, if the order of magnitude is greater or similar, the load is assumed to be dynamic.

### 3.1 Static Analysis

The main static or quasi-static loads acting on the turbine during its operational life can be divided into four different categories based on their nature:

- Pressure loads: the flux of hot gases creates a not uniform pressure distribution on blade surfaces between suction and pressure side. This unbalance causes blade rotation, which is inevitable, considering that the role of the turbine is to extract

energy from the flux to drive the compressor. This load is strictly dependent on the interlocking condition.

- Inertial loads: The system is characterized by high rotational velocity, which generates an inertial load function of rotation radius, material density, rotational speed and of the cross-section on which is applied. In this case, the most stressed area is the blade root, which is, as a consequence, a critical area in the design phase.
- Thermal loads: the hot gases coming from the compressor are characterized by high temperature, and therefore they cause high thermal gradients responsible for creep phenomena. This effect is more common in the High-Pressure Turbine.
- Pre-Twist load: as a consequence of the twist generated by loads on blades during their operation, blades are installed with a pre-load which guarantees the correct positioning of the airfoil with respect to the flux.

The operating condition of the Low-Pressure Turbine is thus obtained taking under consideration the effects of all these loads combined, since they could be responsible for an excessive displacement of the structure, causing interference problems or undesired internal tension. The role of the static analysis is to study the effects of these loads on the structure.

## 3.2 Dynamic Analysis

Turbine vibrations are one of the main failure causes since the rise of resonance phenomena could lead to exceeding the fatigue stress limit of the structure. During the design phase, it is fundamental to evaluate correctly forces and strains acting on the structure, in order to take under consideration fatigue phenomena and thus correctly plan maintenance, assuring a safety margin for the entire operational life. It is particularly important to consider the high-cycle fatigue with highly volatile thermal and mechanical loads depending on rotational velocity and on the fluctuating range of the frequency response. The need to take all these factors into account during the design phase, it's leading towards blading less and less rigid but more loads, thanks also to their materials and production methods enhancement. The final objective is to find an optimal compromise between the need for safety, reliability, efficiency, maintainability, lightness and eco-sustainability.

### 3.2.1 Aeroelasticity

Aeroelasticity studies the iteration between aerodynamic, elastic and inertial forces, whether they are static or dynamic 3.1. Vibration to whom turbine components are subjected are correctly described within this subject, which divides the fields of study into four areas:

- Structure dynamics: Inertial and elastic forces (Structural vibrations)
- Flight mechanics: Inertial and aerodynamic forces (Aerodynamic stability)
- Static aeroelasticity: Elastic and aerodynamic forces (Convergence)
- Dynamic aeroelasticity: Elastic, dynamic and aerodynamic forces (Forced response and flutter)

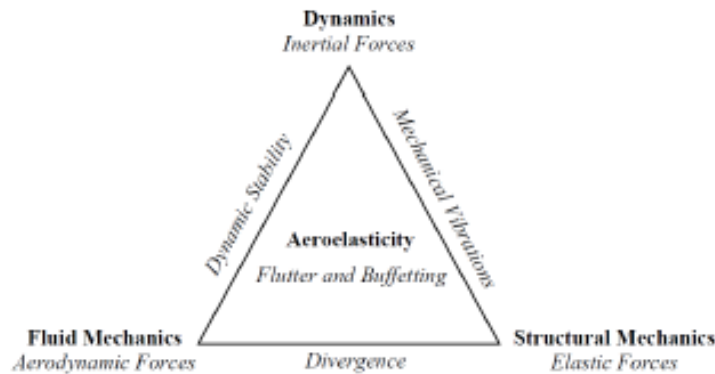


Figure 3.1: Interaction between disciplines [19]

More in-depth considering the dynamic aeroelasticity, a further description of two dynamic phenomena is given:

- Forced response: which analyzes a dynamic system response to an external load, as in this case, the perturbations in the air flux. These disturbances act on blades as exciting forces, showing a harmonic pattern. Its frequency depends on the rotating velocity of the shaft and on the number of blades in adjacent stages.
- Flutter: which studies an intrinsic forcing of the system which shows a self-excited oscillation. The elastic vibration generates aerodynamic forces which sustain or amplify the resulting strain.

These are phenomena acting on the structure, which are amplified by aerodynamic forces that diverge when deformation increases. Divergence is defined as the moment in which

the structure reaches static failure, whilst we talk about flutter when the dynamic instability causes oscillation to the structure up to its breaking.

The dynamic behaviour of the coupled blade-disk system is completely different aerodynamically and mechanically from one of the components isolated. The contact and thus the coupling is characterized by the support type and the shape of the contact surfaces. In order to correctly analyze the structure dynamically, it is necessary to conduct a study of the free vibration and forced response. Furthermore, it's important to verify the high cycle fatigue behaviour (HCF), which can cause component breaking, even if it is characterized by stresses minor to the shear limit of the material. Thus during the design phase, loads to whom the component is subjected during its operational life are considered, in order to define the endurance limit and to avoid failures of the machine.

### 3.2.2 Free Vibration Analysis

This analysis considers the system without external loads, in order to determine the natural frequencies and their damping coefficients, as many as the degrees of freedom (and as a consequence as the number of equations of motion)(fig.3.2).

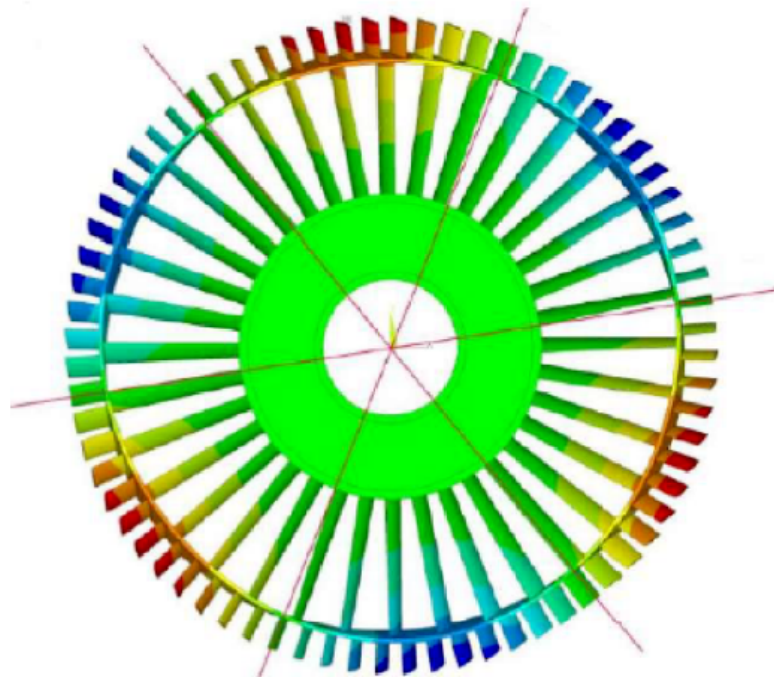


Figure 3.2: Excited blading stage

These elements define the modal properties of the system. The main factors to consider

in the disk-blade system analysis are:

- Rotation around engine axis which creates gyroscopic and centrifugal effects, which increase vibration frequencies because of the stiffness determined by the inertial load.
- Interaction with the flux at a high temperature which modifies material properties, diminishing system stiffness and its vibration frequencies.
- System grade of cyclic symmetry which can be assumed as a set of equivalent segments, thus diminishing computational cost of the analysis.

More in detail, cyclic symmetry determines some types of mode-shapes characterized by some points with null displacement:

- **Nodal diameters:** straight segments
- **Nodal circumferences:** concentric circumferences
- **Stationary modes:** in which all sectors vibrate with equal amplitude and phase, thus described as a single real eigenvector
- **Rotating modes:** characterized by a couple of travelling waves in the same direction, opposed to the disk rotation one.

Since the number of mode-shapes is equivalent to the system number of degrees of freedom, in a real case, there would be infinite mode-shapes, since the system is continuous and not discrete. Results are plotted in the FreND diagram where it is recognizable an increase in the frequencies with the nodal diameter, behavior explained by the enhancement of system tightness with the complexity of mode-shapes. Results are grouped in modal families which can be divided into two main groups:

- System modes:
  1. All the system reacts to deformation during the vibration
- Airfoil modes:
  1. Bending: the blade's nodes move in a plane perpendicular to the turbine axis; the maximum displacement can be observed at midspan
  2. Torsional: the blade's nodes twist around the blade's radial direction, with null displacement at the hub and the tip.

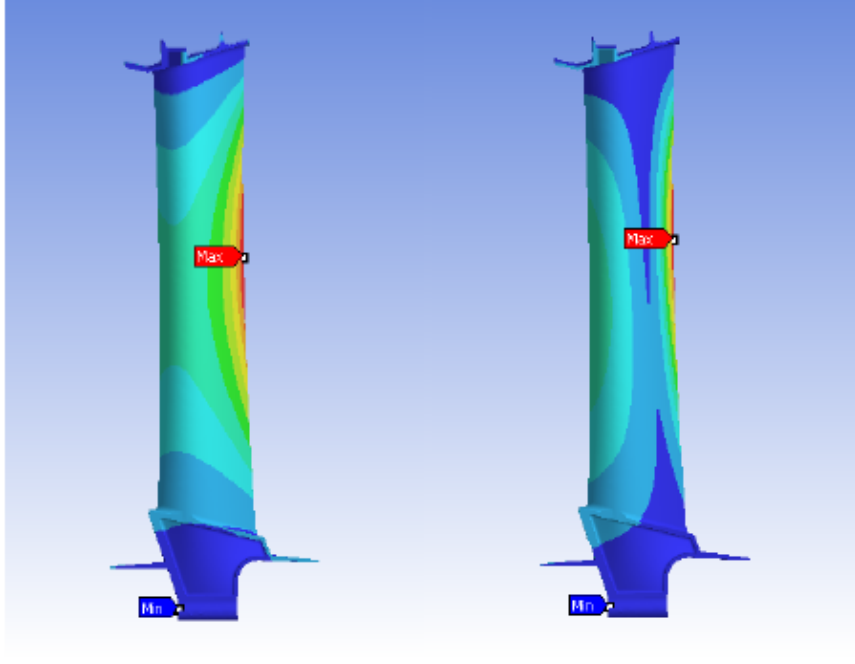


Figure 3.3: Example of bending (left) and torsional (right) modes

### 3.2.3 Forced Response

Forced response analysis takes into account stresses originate by external loads which can cause resonance phenomena. When the amplitudes are elevated, the component could damage or break immediately after a few load cycles. Upstream and downstream components create aerodynamic disturbs, causing the flux to be not-uniform and generating harmonic forces on the blade. Load frequency depends on some characteristics of the system, including rotor rotational velocity, number of blades and number of sectors in which the stator is divided. In order to identify the forcing the Engine Order is used, defined as the ratio between forcing pulsation and rotational speed:

$$EO = \frac{\omega}{\Omega} \quad (3.1)$$

In a fixed reference system or in the frame of the blade, there is a static load. Considering a bladed disk on the plane  $xy$  excited in the fixed point  $\theta^*$  by a normal harmonic force, following the  $z$  direction. The forcing is described with the following equation:

$$\begin{cases} f_{\theta=\theta^*}(t) = F_0 \cos(\omega t) = F_0 \cos(N\Omega t) \\ f_{\theta \neq \theta^*}(t) = 0 \end{cases} \quad (3.2)$$

where  $N$  is the number of blades. The forcing periodicity allows to factorize it using the Fourier series as an infinite sum of harmonic contributes of index  $h$ :

$$f_{\theta}(t) = \frac{F_0}{\pi} \sum_{h=0}^{\infty} \cos[h(\theta - \theta^*)] \cos(\omega t) \quad (3.3)$$

If a rotating reference system is considered, it is necessary to make a variable change as showed in figure 3.4 , thus:

$$\theta = \theta_r + \Omega t \quad (3.4)$$

As a consequence, the Fourier series expansion modify as follows:

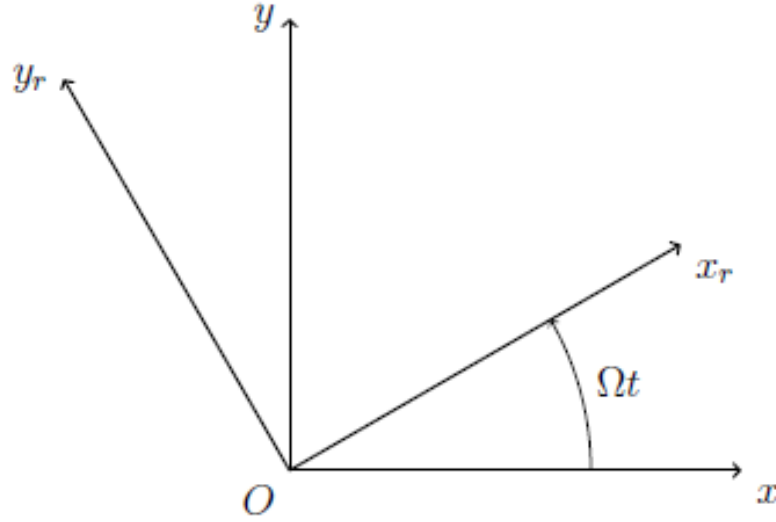


Figure 3.4: Variable change in order to pass from a fixed to a rotating system

$$f_{\theta,r}(t) = \frac{F_0}{2\pi} \sum_{h=0}^{\infty} \{ \cos[(\omega - h\Omega)t] \cos(h\theta_r) + \sin[(\omega - h\Omega)t] \sin(h\theta_r) + \cos[(\omega + h\Omega)t] \cos(h\theta_r) - \sin[(\omega + h\Omega)t] \sin(h\theta_r) \} \quad (3.5)$$

The single blade results to be subjected to two different forces for each EO:

- *forward travelling force* in the same direction of the rotational speed of the bladed disk
- *backward travelling force* which rotates in counter direction with respect to angular velocity of the disk

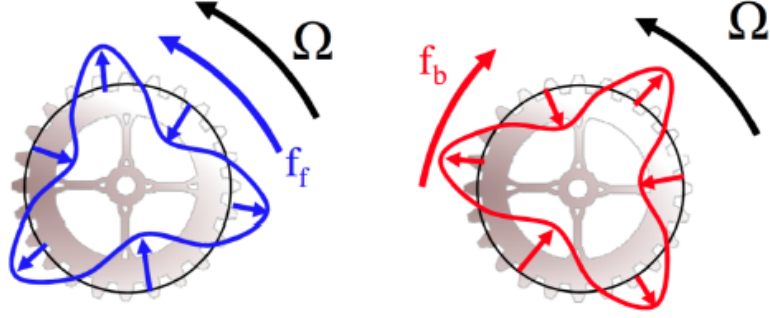


Figure 3.5: Forward and backward forces [16]

Frequencies of the forces respectively are:

$$\omega_f = \omega - h\Omega \quad (3.6)$$

$$\omega_b = \omega + h\Omega \quad (3.7)$$

Therefore the exciting frequencies are function of the forcing pulsation  $\omega$ , of the number of sectors  $N$  and of the harmonic index  $h$ :

$$\Omega_f = \omega(N - h) \quad (3.8)$$

$$\Omega_b = \omega(N + h) \quad (3.9)$$

Thus the corresponding EO assume the following equation:

$$EO_f = \frac{\Omega_f}{\omega} = N - h \quad (3.10)$$

$$EO_b = \frac{\Omega_b}{\omega} = N + h \quad (3.11)$$

A relevant contribution to the study of forced response was given by Wilfred Campbell. The homonymous diagram allows identifying resonance conditions of a turbo-machine. This event occurs when the frequency of the periodic forcing acting on a mechanical system is close to the natural frequency of the system, which causes high amplitude vibrations, particularly damaging for the component. The Campbell diagram has on the axis of abscissa the rotational velocity of the rotor, and on the y-axis frequency. Thus, natural frequencies of the bladed-disk are represented as horizontal lines, whereas the forcing frequency trend is described as lines with an inclination increasing with EO. In figure 3.6 the highlighted points are intersection points between the natural frequencies trend and the lines of the forcing conditions, identifying resonance conditions, ruled in

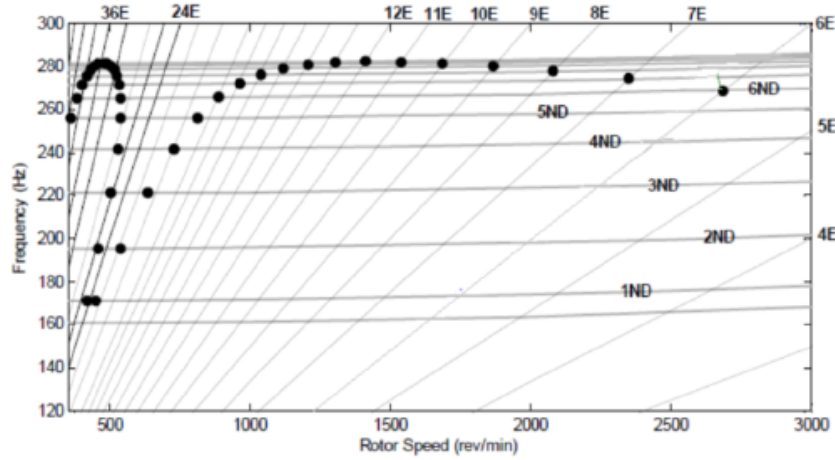


Figure 3.6: Campbell diagram [10]

the diagram by the following expression:

$$EO = mN \pm h \quad \forall m \in \mathbb{N} \quad (3.12)$$

where  $h$  is the nodal diameter and  $N$  the number of blades. The aim of engineers is to avoid that resonance conditions are close to the main operating conditions of the engine, in order to limit damaging conditions of vibration. To this end, engineers act on either rotational speed or natural frequencies. Usually, it is easier to manipulate the second parameter, by changing the dimensions of some critical components in order to change their natural frequencies, moving them away from the engine orders at the operational velocity. Finally, forced response problems may be related both to an aerodynamically induced vibration due to variable pressure field or to mechanical induced vibration related to shaft unbalance level.

### 3.2.4 Flutter

With the term flutter are identified the structure self-excited and sustained phenomena which rises at the natural frequencies of the system according to its vibration modes. In certain cases non-stationary aerodynamic forces originated by oscillation could be high enough to affect the vibrating pattern of the system, moving it away from free response conditions in terms of frequency and vibrating modes. In facts, flutter can influence mode-shapes: wings generally show a flutter behaviour characterized by a coupling between flexional and torsional, whereas turbine blades show a single mode with a frequency similar to the free-response.

If the system is not correctly damped, oscillation increase quickly up to breaking. This condition is reached because, once the vibration starts, the kinetic energy of the flux that excites it is greater than the energy that the structure can absorb. The reason why it is necessary to evaluate the damping requires is that the aerodynamic force is not in-phase with the vibrating pattern of the structure (fig.3.7).

There is another critical point to consider in the design of turbine stages; indeed, each

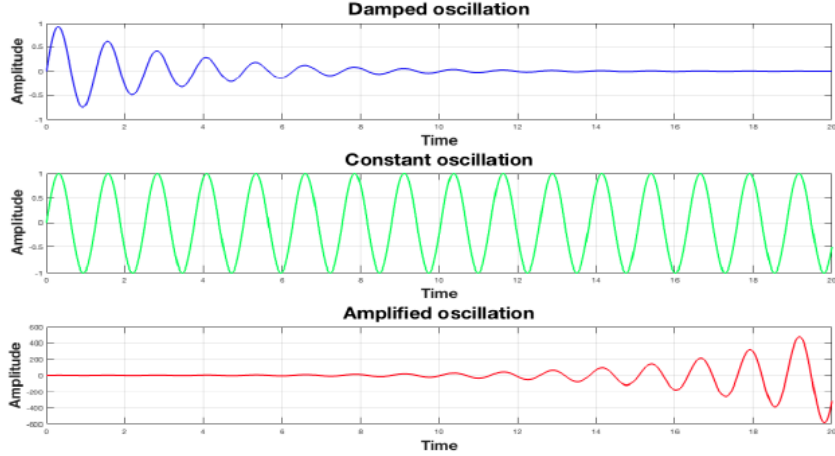


Figure 3.7: Flutter oscillation

of them is influenced by the previous and the following, causing the rising of common properties and behaviours. For example, turbine stages are coupled mechanically and vibrate at the same frequency, but with a phase shift equals to:

$$IBPA = \frac{2\pi n}{N} \quad (3.13)$$

where  $n$  is the nodal diameter and  $N$  is the number of blades of the stage. It's clear how blades influence each other creating effects result of a combination between each perturbation field. This behaviour is commonly analyzed through energy and work analysis:

$$L_a = \int_t^{t+\Delta t} \int_S -p\vec{n} \cdot v dS dt \quad (3.14)$$

where  $S$  is the blade surface,  $v$  the velocity associated to the mode,  $\vec{n}$  the unitary vector of the surface. From here it is possible to evaluate the critical damping factor:

$$\zeta = \frac{-L_a}{8\pi E} \quad (3.15)$$

where  $E$  the kinetic energy of the blade is:

$$E = \frac{1}{4}m\omega_n^2 a^2 \quad (3.16)$$

where  $m$  modal mass and  $a$  vibration amplitude.

### 3.3 Cyclic Symmetry

The equilibrium equation of the structure under an external load is:

$$[M] \cdot \{\ddot{x}\} + [C] \cdot \{\dot{x}\} + [K] \cdot \{x\} = \{F\} \quad (3.17)$$

where  $[M]$ ,  $[C]$  and  $[K]$  are respectively the mass, damping and stiffness matrices of the structure,  $\{x\}$  is the vector of the DOF and  $\{F\}$  is the external loads vectors applied to the system. The number of nodes  $n_n$  derived from structure discretization determines the dimension of vectors and matrices that appear in the equation of motion:  $[M]$  and  $[K]$  are squared matrices  $3n_n \times 3n_n$ ,  $\{x\}$  and  $\{F\}$  column vectors  $3n_n \times 1$ .

As aforementioned cycle symmetric structures can be divided into a finite number  $N$  of sectors, each one with  $n_s$  degrees of freedom. Therefore, given a cylindrical reference system with axis  $\rho, \theta$  and  $z$  (coincident with engine axis), the equation of motion can be rewritten in such a way that the  $n_s$  degrees of freedom of a sector are followed by the ones of the adjacent sector. By applying the same convention to the forces vector:

$$\{x\} = \begin{Bmatrix} x_1 \\ x_2 \\ x_3 \\ \vdots \\ x_{N-1} \\ x_N \end{Bmatrix} \quad \{F\} = \begin{Bmatrix} F_1 \\ F_2 \\ F_3 \\ \vdots \\ F_{N-1} \\ F_N \end{Bmatrix} \quad (3.18)$$

Therefore  $\{x\}$  and  $\{F\}$  are composed of  $N$  sub-vectors, each one with DOF of the sector it refers to. If the DOF counterpart hold the same position in each sub-vector  $\{x_i\}$ , with

$i = 1, \dots, N$ , mass and stiffness matrices show a symmetric composition:

$$[M] = \begin{bmatrix} M_0 & M_1 & M_2 & \cdots & M_2 & M_1 \\ M_1 & M_0 & M_1 & \cdots & M_3 & M_2 \\ M_2 & M_1 & M_0 & \cdots & M_4 & M_3 \\ \vdots & \vdots & \vdots & \ddots & \vdots & \vdots \\ M_2 & M_3 & M_4 & \cdots & M_0 & M_1 \\ M_1 & M_2 & M_3 & \cdots & M_1 & M_0 \end{bmatrix} \quad (3.19)$$

$$[K] = \begin{bmatrix} K_0 & K_1 & K_2 & \cdots & K_2 & K_1 \\ K_1 & K_0 & K_1 & \cdots & K_3 & K_2 \\ K_2 & K_1 & K_0 & \cdots & K_4 & K_3 \\ \vdots & \vdots & \vdots & \ddots & \vdots & \vdots \\ K_2 & K_3 & K_4 & \cdots & K_0 & K_1 \\ K_1 & K_2 & K_3 & \cdots & K_1 & K_0 \end{bmatrix} \quad (3.20)$$

The blocks  $[M_h]$  and  $[K_h]$  (with  $h = 0, \dots, N/2$  if  $N$  is even and  $h = 0, \dots, (N - 1)/2$  if  $N$  is odd), they are in turn symmetrical matrices with size  $n_s \times n_s$ . Since the structure is in cyclic symmetry, each sector of the bladed disk is bound to the adjacent: from a mathematical perspective, this means non-null element outside the diagonal.

The modal analysis consists of the solution of the non-damped system and in the resolution of the eigenvalues problem, in order to obtain the decoupled equations of motion, which gives the opportunity to describe a  $n - DOF$  vibrating system as a combination of  $n$  independent one-DOF systems.

The homogeneous equation of motion can be written as:

$$([K] - \omega^2 \cdot [M]) \cdot \{\psi\} = \{0\} \quad (3.21)$$

where  $\omega$  represents the eigenvalue (or natural frequency) and  $\{\psi\}$  represents the corresponding eigenvector (or mode shape). In the analysis, in order to obtain valid results, it is important to guarantee a very fine mesh which means a high computational cost. In order to diminish the analysis time, usually, just a single sector of the disk-blade system is considered. This simplification is possible thanks to the assumption of cyclic symmetry (fig. 3.8) and the application of its boundary conditions, which is applicable only if there is perfect equality with the previous and the following component. With this method, it is therefore possible to exploit the rotational periodicity of disk-blade turbine systems. The fundamental sector has three different types of nodes, represented in the following figure:

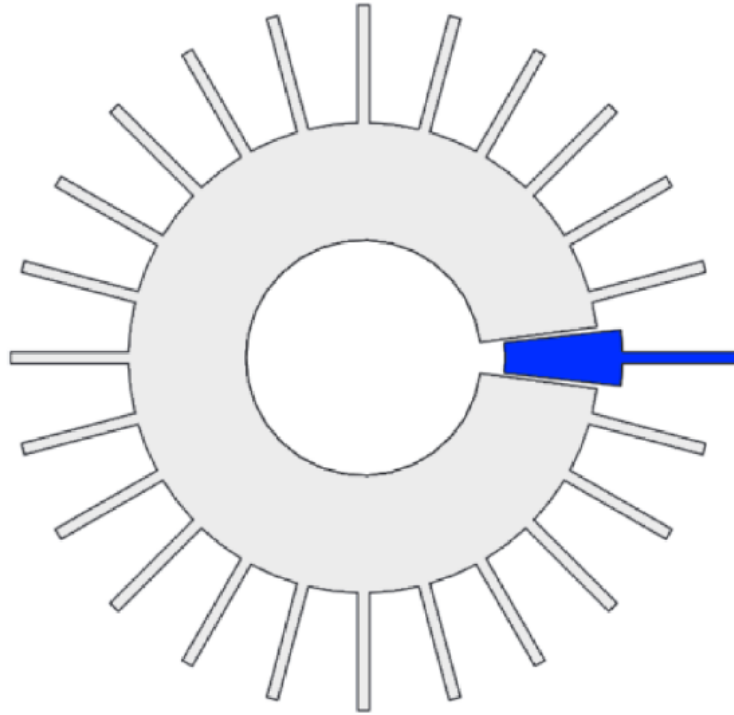


Figure 3.8: Cyclic symmetry

- Right-hand side nodes (called R) which are the nodes which are the ones in common with the sector on the right
- Left-hand side nodes (called L) which are in common with the neighbour sector on the left
- Inner node (called I) which are the nodes in the contact area.

The cyclic symmetry condition is applied between the Right(R) and Left(L) nodes with respect to the engine axis  $z$ . The solution vector, which contains the DOFs of the sector, can be rearranged as follows:

$$\{x\} = \begin{Bmatrix} \{x_R^s\} \\ \{x_L^s\} \\ \{x_I^s\} \end{Bmatrix} \quad (3.22)$$

At the same way the forces acting on the sector can be expressed as:

$$\{F\} = \begin{Bmatrix} \{F_R\} \\ \{F_L\} \\ \{F_I\} \end{Bmatrix} \quad (3.23)$$

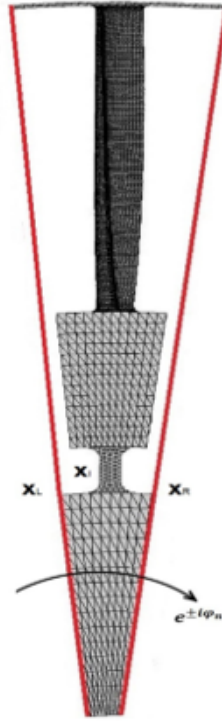


Figure 3.9: Cyclic symmetry conditions

Thus, without considering damping, the non-homogeneous equation of motion can be rearranged as follows:

$$([K^s] - \omega^2 \cdot [M^s]) \cdot \{x^s\} = \{F\} \quad (3.24)$$

The resulting solution for the chosen sector is still valid for all the others, taking under consideration the phase-shift described before (IBPA), which allows to connect the solution of the right nodes with the left-hand ones:

$$\{x_R^s\} = \{x_L^s\} \cdot e^{j\phi} \quad (3.25)$$

thus resulting in the corresponding solution vector:

$$\{x\} = \begin{Bmatrix} \{x_L^s \cdot e^{j\phi}\} \\ \{x_L^s\} \\ \{x_I^s\} \end{Bmatrix} \quad (3.26)$$

The equation 3.25 can be written in Euler notation as follows:

$$\{x_R^s\} = \{x_L^s\} \cdot e^{j\phi} = \{x_L^s\} \cdot \left( \cos\left(\frac{2\pi \cdot n}{N}\right) + j \sin\left(\frac{2\pi \cdot n}{N}\right) \right) \quad (3.27)$$

in which is clear that for certain values of IBPA, like  $n = 0$ , the imaginary part of the solution is null, thus resulting in a real solution of the eigenvalues problem.

### 3.4 Modal Analysis

The modal analysis allows determining natural frequencies and the mode shapes of the structure. Given the aforementioned cyclic symmetry properties of rotors as the bladed disk, it is possible to analyze a unique sector, by introducing the relative constraints already described, in such a way that it correctly represents the behaviour of the entire structure. This and other reduction techniques (ROM, Reduced Order Modeling) allow to consistently abate computational cost that would be associated with the analysis of the entire rotor.

There are different method to conduct the modal analysis of a cycle symmetric structure, among the others, the one proposed by D.J.Mead. Given  $\{x_s\}$  the DOF vector of the fundamental  $n$ th-sector (fig. ) described as follows:

$$\{x_s\} = \begin{Bmatrix} x_l \\ x_i \\ x_r \end{Bmatrix} \quad (3.28)$$

where  $\{x_l\}$  represents the vector of the  $3_{n_l}$  degrees of freedom of the left interface of the sector chosen, which are in common with the  $(n - 1)$ th-sector;  $\{x_l\}$  refers to the  $3_{n_r}$  DOF of the right interface of the fundamental sector; finally  $\{x_i\}$  which refers to the  $3_{n_i}$  inner DOF, which are exclusively part of the reference sector. In order to impose cyclic symmetry, the number of degrees of freedom of the right interface has to be equal to the number of DOF of the left one, thus  $3_{n_r} = 3_{n_l}$ .

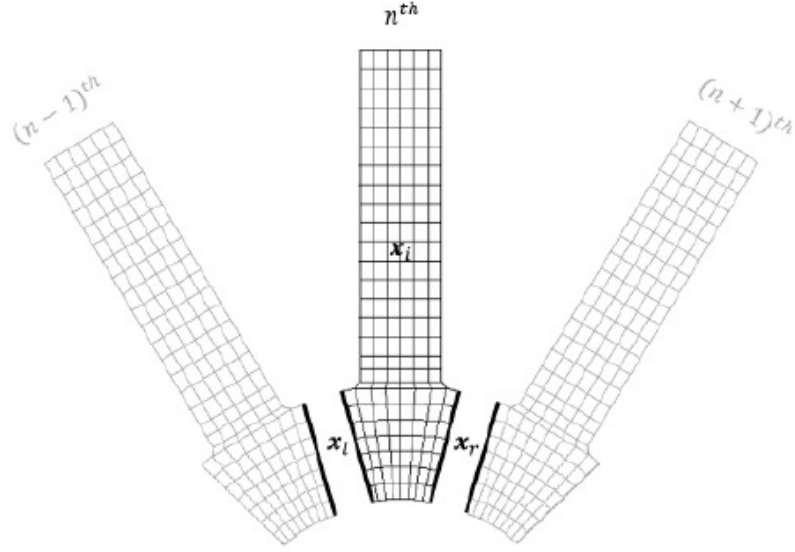


Figure 3.10: DOF division in the  $n$ th-sector

The external loads vector division is equivalent to the one of the degrees of freedom:

$$\{f_s\} = \begin{Bmatrix} f_l \\ f_i \\ f_r \end{Bmatrix} \quad (3.29)$$

The mass and stiffness matrices of the single sector that appear in the equation of motion (3.17) can be rewritten in order to respect the degrees of freedom partition:

$$[M_s] = \begin{bmatrix} M_{ll} & M_{li} & M_{lr} \\ M_{il} & M_{ii} & M_{ir} \\ M_{lr} & M_{ri} & M_{rr} \end{bmatrix} \quad (3.30)$$

$$[K_s] = \begin{bmatrix} K_{ll} & K_{li} & K_{lr} \\ K_{il} & K_{ii} & K_{ir} \\ K_{lr} & K_{ri} & K_{rr} \end{bmatrix} \quad (3.31)$$

and then it is necessary to impose the conditions of:

- continuity, displacement of the right interface of the  $n$ th-sector has to be equal to the displacement of the left interface of the following sector

$$\{x_r\}_n = \{x_l\}_{n+1} \quad (3.32)$$

- equilibrium, given by the following relation between forces

$$\{f_r\}_n = -\{f_l\}_{n+1} \quad (3.33)$$

The cyclic symmetry property of the rotor requires that corresponding nodes of right and left interfaces oscillate one to the other with a phase shift equals to the IBPA. Considering the degrees of freedom of the left interface as independent, the following relation is obtained:

$$\{x_r\} = \{x_l\}e^{i\varphi_h} \quad (3.34)$$

The independent DOF are kept also after the reduction. Similar considerations are valid for the forces:

$$\{f_r\} = -\{f_l\}e^{i\varphi_h} \quad (3.35)$$

As a consequence, the degrees of freedom vector can be rewritten as:

$$\{x_s\} = \begin{Bmatrix} x_l \\ x_i \\ x_r \end{Bmatrix} = \begin{bmatrix} I & 0 \\ 0 & I \\ Ie^{i\varphi_h} & 0 \end{bmatrix} = [T^h] \begin{Bmatrix} x_l^h \\ x_i^h \end{Bmatrix} \quad (3.36)$$

where:

- $[T^h]$  is the transformation matrix
- $[(x_l^h)^T \quad (x_i^h)^T]^T$  is the degrees of freedom vector reduced in cyclic symmetry referred to the nodal diameter  $h$ .

The transformation leads to rewriting the eigenvalues problem for a given  $\varphi_h$ :

$$([K^h] - \omega_i^2[M^h])\{z_i^h\} = 0 \quad (3.37)$$

with

$$[M^h] = [T^h]^T[M][T^h] \quad [K^h] = [T^h]^T[K][T^h] \quad (3.38)$$

The computational cost abates significantly since the number of degrees of freedom decreases from  $3(2n_l + n_i)$  to  $3(n_l + n_i)$  for the reduced problem. The value of  $\varphi_h$  determines the phase shift between the sectors. To each IBPA corresponds more mode shapes, and each one has the same phase shift among sectors. Varying  $\varphi_h$  in its admissible values, all the mode shapes of the structure are obtained, even if just a single sector was considered.

### 3.4.1 Modeshapes

The solution of the eigenvalues problem provides the resonant frequencies and the corresponding mode shapes. The mode shape, regardless of its class, it is always describable as a sum of harmonic functions as  $\sin(h\theta)$  and  $\cos(h\theta)$ , in which  $\theta$  is the tangential coordinate of the structure in cyclic symmetry;  $h$  or  $ND$  is the nodal diameter, which carries information about the periodicity of the mode shape.

The number of nodal diameters in a rotor depends on its number of sectors  $N$  in cyclic symmetry, following the rule:

$$\begin{cases} 0 \leq h \leq \frac{N}{2} & \text{if } N \text{ is even} \\ 0 \leq h \leq \frac{N-1}{2} & \text{if } N \text{ is odd} \end{cases} \quad (3.39)$$

The combination between the number of ND and NC results in the following vibration modes:

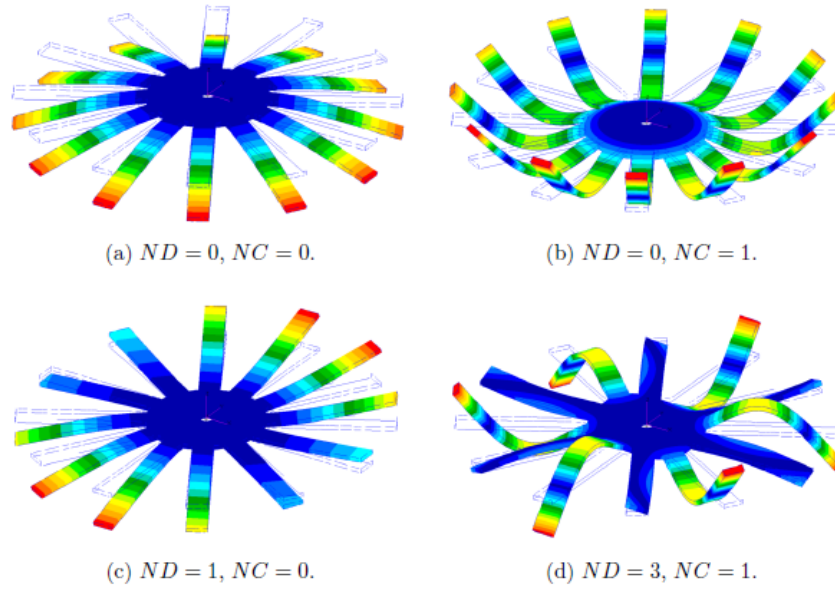


**Figure 3.11: Bladed disk vibration modes at vary nodal diameters (ND) and nodal circumferences (NC) [4]**

Once the nodal diameter  $h$  is assigned, the IBPA is calculated through equation 3.13, and then we can distinguish among three different types of vibration:

- **Standing wave** (stationary mode): when  $ND = 0$  or  $ND = \frac{N}{2}$ , in this condition all the blades vibrate at the same phase, frequency and amplitude, therefore one eigenvector is enough to describe the entire vibration pattern. Considering two

corresponding points on different sectors, the displacement is the same in every moment.

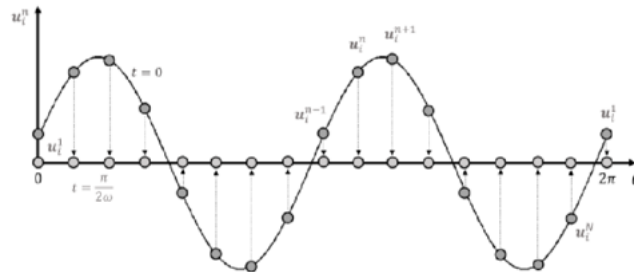


Figure 3.12: Standing wave

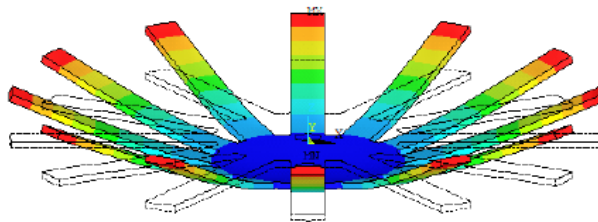


Figure 3.13: Stationary mode [6]

- Rotating mode:** it occurs when the number of ND is non-zero and the consequent effect is the one of having two waves that rotates on opposite directions. This means that adjacent sectors move with different phases, each mode-shape is described with a couple of orthogonal eigenvectors and a pair of the corresponding eigenvalues. More in depth, the wave that rotates following the rotational speed is called forward. By contrast, the one rotating in the counter direction is called backward.

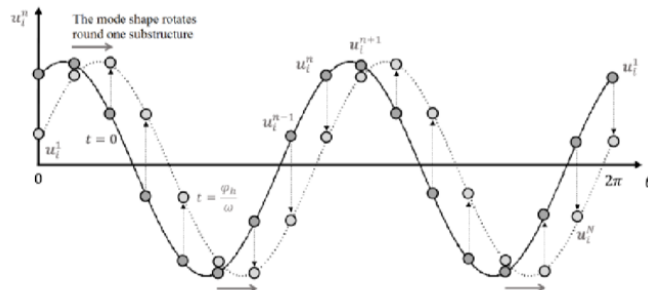


Figure 3.14: Rotating wave

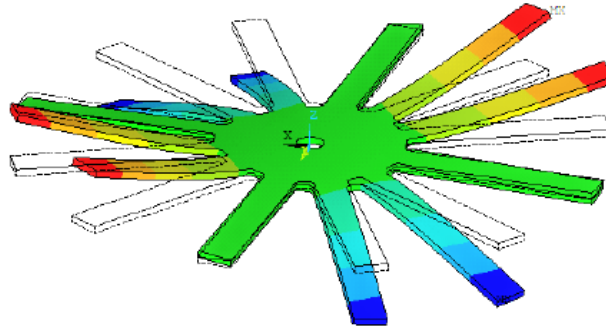


Figure 3.15: Rotating mode [6]

### 3.4.2 FreND Diagram

A continuous system has an infinite number of DOFs, thus resulting in an infinite number of mode-shapes, each one associated to a specific nodal diameter and frequency. But the modeling phase through FE results, models the structure in a finite number of DOF since the number of nodes itself is finite. In the engineering practice, since turbines in their operating life face a relatively small range of frequencies, just first natural frequencies are considered. Therefore on a Campbell diagram we would find a large amount of crossing between external excitation and natural frequencies. However, each crossing does not necessarily represent a dangerous situation, because it is important to take under consideration both frequency and mode-shape to have resonance. The FreND diagram allows to give a further classification in order to identify dangerous conditions.

The representation of the dynamic behavior is obtained using the FreND diagram (Frequency vs Nodal Diameter): which classifies frequencies depending on their nodal diameter (fig. 3.16). As nodal diameter grows, there is an increase of the mode shapes natural frequencies and aims to a horizontal asymptote. In fact, since the nodal diameter is the number of lines with null-displacement passing through the centre of the circumference, the higher the nodal diameters number the greater structure stiffness, causing the rise of more complex mode-shapes. At low nodal diameters, there is a prevalence for disk mode-shapes; by contrast, at high ND blade mode-shapes are the main ones. This means that in the first case, the disk displacement causes the blade displacement, whereas, at high ND, the disk can be assumed rigid and therefore the deformation is mainly in the blades.

The classification of the results of a modal analysis on the FreND diagram can be based on frequency or modal shape. In the first case, on equal nodal diameter, the mode is individuated by frequency. By contrast, the modal classification associates frequencies to a certain modal family given by the deformed shape of the structure (mode 1, mode

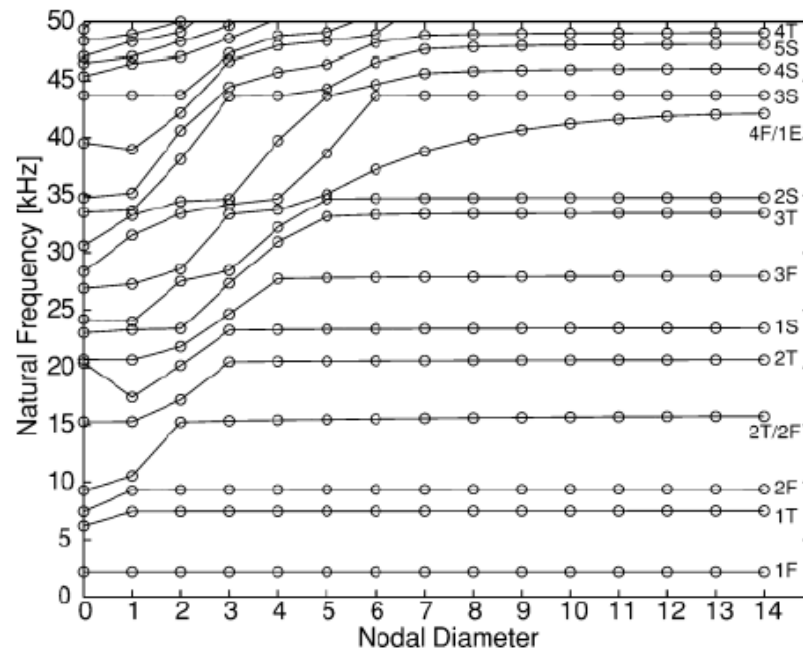


Figure 3.16: FreND diagram [8]

2, ...). In some cases, there is the *veering* zone in the FreND diagram, which is a region where two modal families interchange mode shapes, showing a crossing of the natural frequencies.

## Chapter 4

# Introduction to Signal Analysis

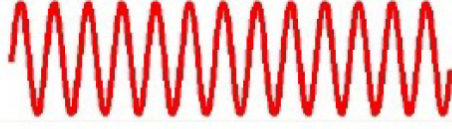
Up to this point, an introduction to rotor dynamics has been given, allowing the reader to better understand the components analyzed during this thesis work and their physical characteristics. From now, an insight into the frequency analysis is given, which represents the main theme faced during these months, and it underlies both the development of the code and its application to the test cases.

### 4.1 Signal Classification

Classification of signals is necessary in order to differentiate among the various parameters to consider in the analysis phase. First of all, each signal can be classified as stationary or non-stationary. Where the former group is, for example, the result of a test conducted at a constant speed, in such a way that the frequency content is stationary over time, whereas the latter is often the output of a system going through acceleration or deceleration phases. Another important condition to define a signal as stationary, is the average value, which has to be constant over time and independent from the sampling period,

A further classification within stationary signals is between deterministic, in which output can be correctly predicted from the input received, and random signals (fig. 4.1), where there isn't a direct correlation between input and output, but since they are classified as stationary signals, their mean, variance and other statistical properties are constant over time.

### Deterministic



### Random



Figure 4.1: Stationary signals division

By contrast, non-stationary signals can be divided in transient signals, which begin and end at zero, and continuous signals in which this does not happen.

#### 4.1.1 Fourier Transform

The Fourier theorem states that every periodic signal can be represented as a infinite sum of sine and cosine functions with variable amplitude, phase and period, which is called Fourier series.

The Fourier series is defined as follows:

$$x(t) = a_0 + \sum_{n=1}^{\infty} \left[ a_n \cos \left( n \frac{2\pi}{T} t \right) + b_n \sin \left( n \frac{2\pi}{T} t \right) \right] \quad (4.1)$$

In order to correctly represent a signal using the Fourier series, it is necessary to determine each  $n$  term. The amplitude of the  $n^{\text{th}}$  harmonic is controlled by the Fourier coefficients  $a_n$  and  $b_n$ , defined as follows:

$$a_n = \frac{2}{T} \int_{-\frac{T}{2}}^{+\frac{T}{2}} x(t) \cos \left( n \frac{2\pi}{T} t \right) dt \quad (4.2)$$

$$b_n = \frac{2}{T} \int_{-\frac{T}{2}}^{+\frac{T}{2}} x(t) \sin \left( n \frac{2\pi}{T} t \right) dt \quad (4.3)$$

where  $T$  is the interval in which the signal is defined.

The objective of signal analysis is to identify the frequency content of the signal and their

contribution to the overall amplitude, which means to obtain the frequency spectrum of a signal starting from its temporal trend. For example, in fig. 4.2 is presented a signal originated by the first three harmonics of the Fourier series of a square wave, described by the following equation:

$$f(x) = \frac{4}{\pi} \sum_{n=1,3,5,\dots}^{\infty} \frac{1}{n} \sin\left(\frac{n\pi x}{L}\right) \quad (4.4)$$

where  $2L$  is the length of the square wave, and  $n$  is the index identifying the harmonics. In the plot, it is possible to identify both the sum of the three components in the time

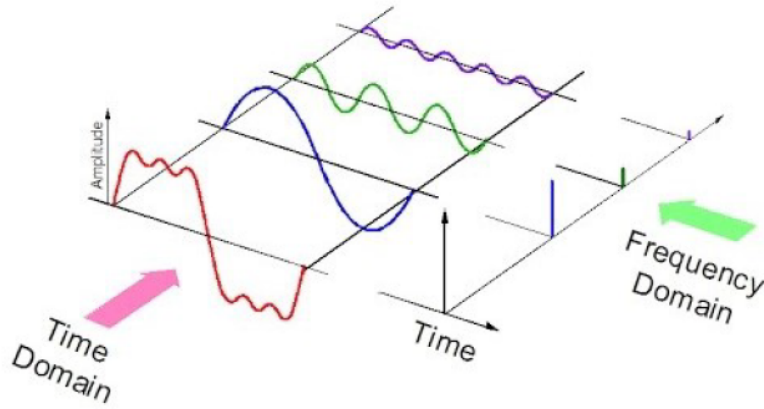


Figure 4.2: Time domain and Frequency domain

domain and the frequency domain representation which gives the result of applying the Fourier transform to the signal: the frequency spectrum, which represents the amplitude of the periodic components. Thanks to this method, it is immediate to understand which harmonics contribute the most to the overall amplitude of the signal.

Here another basic example of the Fourier transform application is given: let us consider a signal  $S(t)$  sampled at a sampling frequency  $F_s = 1000 \text{ Hz}$  obtained by summing three sine signals respectively of frequency  $20 \text{ Hz}$ ,  $60 \text{ Hz}$  and  $85 \text{ Hz}$  (fig. 4.3, 4.4):

$$S(t) = 0.7\sin(2\pi \cdot 20 \cdot t) + \sin(2\pi \cdot 60 \cdot t) + \sin(2\pi \cdot 85 \cdot t) \quad (4.5)$$

In figure 4.4 the overall signal is showed, and this gives a clear understanding of the result of combining different harmonics together. Furthermore, in a real case, a combination of harmonics is usually not enough to describe a specific signal in the time domain, which usually has a further random noise (fig. 4.5). But already looking to the signal obtained by the sum of three simple harmonics at a known frequency, it is clearly hard

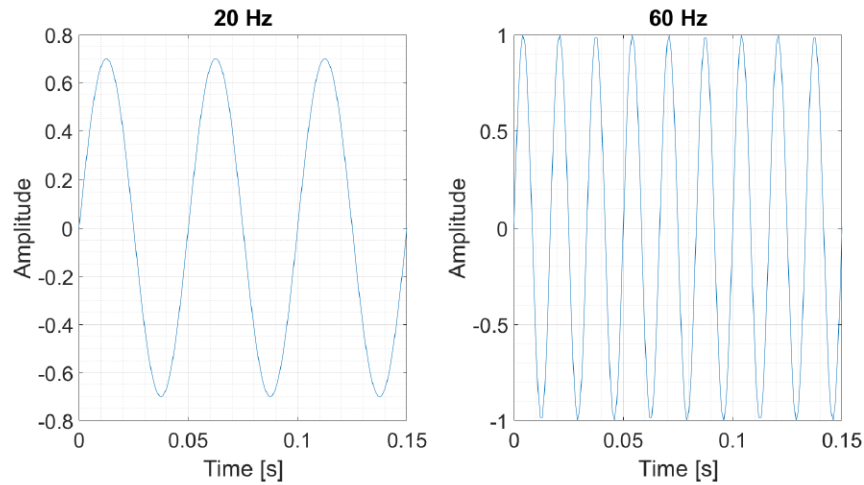


Figure 4.3: Sine waves composing the signal with frequencies of 20 and 60 Hz [7]

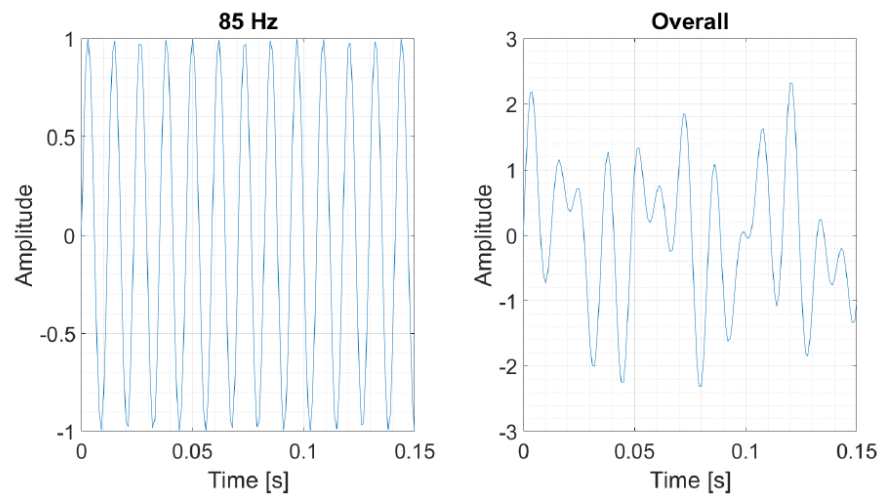


Figure 4.4: Sine waves composing the signal with frequencies of 20 and 60 Hz [7]

to trace it back to its basic harmonics. The Fourier transform is a powerful tool that allows identifying the frequency of the periodic waves composing the signal. In figure 4.6 the spectrum of the signal  $S(t)$  is shown. It is obtained through the Fast Fourier Transform (FFT), which is a specific algorithm, usually employed by calculators, which executes the Fourier Transform. Generally, a signal has both a positive and negative frequency spectrum, which are symmetrical to the y-axis. Therefore, displaying both sides is redundant, but it is important to take into consideration that half the energy of the signal is contained in the negative part of the spectrum. Thus, the positive values of the frequency spectrum have to be doubled, for more information on this matter see [9].

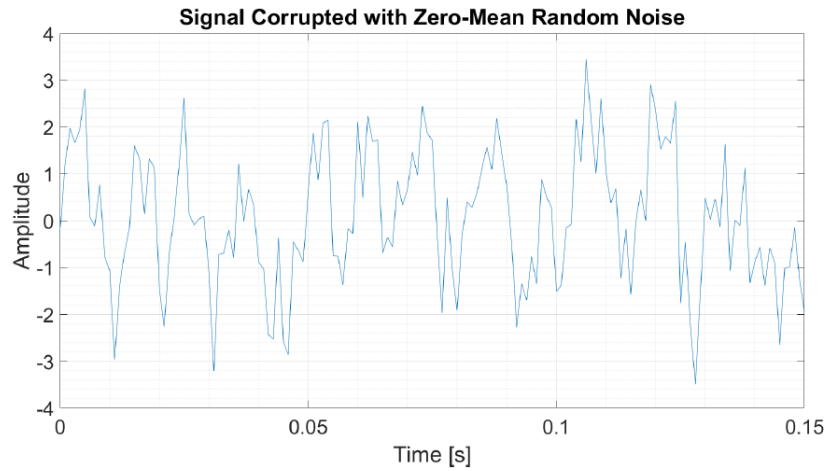
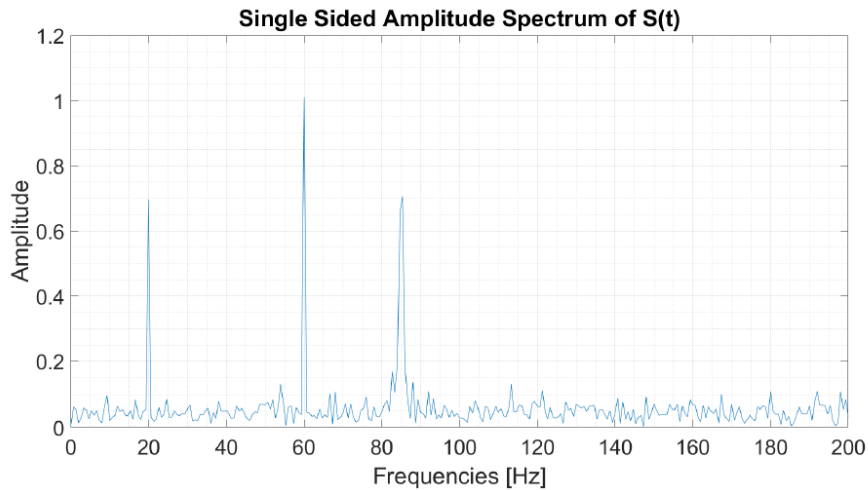


Figure 4.5: Signal with random noise added [7]

Figure 4.6: Spectrum of the signal  $S(t)$  [7]

Thanks to the Fourier transform, it is now evident that there are three main frequencies components, which are, as expected at 20, 60 and 85 Hz. It is interesting to notice that the spectrum accurately identifies the amplitude of the two sine waves (0.7 and 1 from equation 4.5), but not the one at 85 Hz. This error is due to the so-called spectral leakage, which will be further explained later on.

The Fourier transform, given a time-dependent signal  $x(t)$ , calculates its frequency spectrum  $X(f)$  as follows:

$$X(f) = \int_{-\infty}^{+\infty} x(t)e^{-j2\pi ft} dt \quad (4.6)$$

where the exponential represents the frequency  $f$  contribution to the signal  $S(t)$ . This formulation is applicable for continuous signals which extends infinitely in the time domain.

The inverse transformation is:

$$x(t) = \int_{-\infty}^{+\infty} X(f)e^{j2\pi ft} dt \quad (4.7)$$

which vice versa allows representing a continuous signal as the sum of an infinite number of periodic exponential weighted by  $X(f)df$ . Since  $X(f)$  is usually complex, it is described by an amplitude and a phase spectrum.

Obviously, it is impossible to integrate over an infinite time interval using a calculator; it is therefore necessary not to respect the continuity hypothesis. In order to perform the Fourier transform, the signal is discretized into a finite number of values both in time and frequency domain. Therefore, the signal is truncated into small time intervals, transforming the integral of equation 4.6 into a finite summation of terms. The calculator then applies the Discrete Fourier Transform (DFT) which grants a sufficiently precise approximation of the Fourier Transform:

$$X(kf_0) = \frac{1}{N} \sum_{n=0}^{N-1} x(nT_0)e^{-\frac{j2\pi kn}{N}} \quad (4.8)$$

and its inverse transform is:

$$x(nT_0) = \sum_{k=0}^{N-1} X(kf_0)e^{-\frac{j2\pi kn}{N}} \quad (4.9)$$

## 4.2 Signal Preprocessing

Before applying the DFT, the analogue signal has to undergo the following steps:

1. sampling
2. truncation
3. frequency discretization

### 4.2.1 Sampling

Sampling a continuous analogue signal  $x(t)$  consists of measuring its values  $x(iT_s)$  at given time instants  $iT_s$ , with a time interval of measurement defined by the sampling frequency  $F_s$ , which is the number of samples for recording second. Considering an ideal

impulse train, it is possible to easily show how sampling works and its main properties. In figure 4.7 a generic continuous signal  $x(t)$  is showed, with its frequency spectrum  $X(f)$  limited up to frequency  $f_m$ . To sample a signal means ideally to multiply it by an impulse train  $s(t)$  shown in figure 4.8 , whose frequency spectrum is given in figure 4.9, the single pulses are separated by  $F_s$  frequencies.

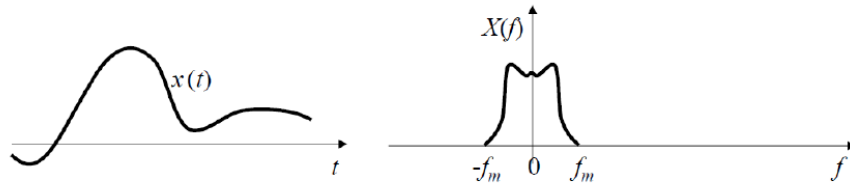


Figure 4.7: Generic signal with a limited bandwidth

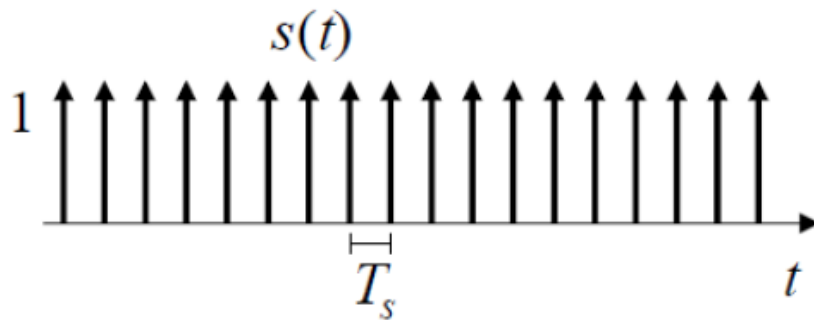


Figure 4.8: Pulse train in time domain

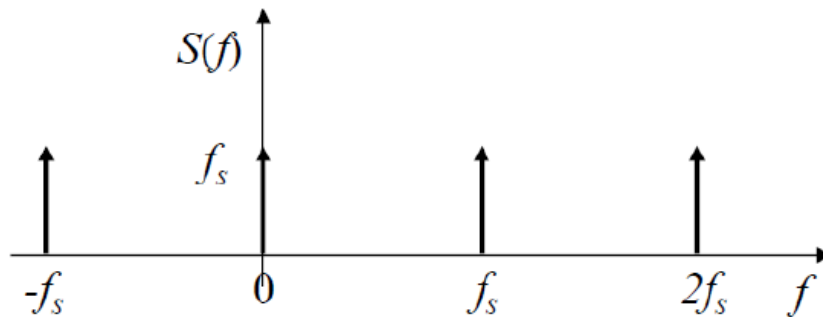


Figure 4.9: Pulse train in frequency domain

The impulse train in the time domain is defined as:

$$s(t) = \sum_{i=-\infty}^{+\infty} \delta(t - iT_s) \quad (4.10)$$

whereas in the frequency domain:

$$S(f) = f_s \sum_{k=-\infty}^{+\infty} \delta(f - kf_s) \quad (4.11)$$

And as aforementioned, the sampling of the signal is obtained by multiplying it with the train impulse in the time domain:

$$x_s(t) = x(t) \cdot s(t) = x(t) \sum_{i=-\infty}^{+\infty} x(iT_s)\delta(t - iT_s) \quad (4.12)$$

which is shown in figure 4.10, while in the frequency domain multiplication is equivalent to a convolution between  $X(f)$  and  $S(f)$  is

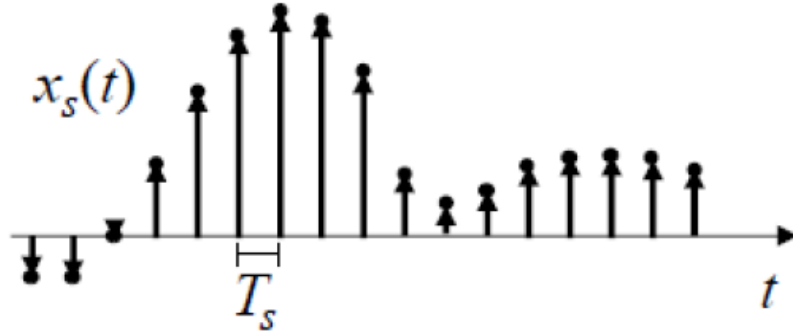


**Figure 4.10: Sampled signal in time domain**

$$X_s = X(f) * S(f) = X(f) * f_s \sum_{k=-\infty}^{+\infty} \delta(f - kf_s) = f_s \sum_{k=-\infty}^{+\infty} X(f - kf_s) \quad (4.13)$$

The result of the sampling procedure is shown in figure 4.10 and 4.12. The signal frequency spectrum, once it has been subjected to the sampling phase, consists of repetitions of the original signal spectrum  $X(f)$ , offset to multiple of the sampling frequency  $F_s$ . In order to avoid overlap between the repetitions, the separating frequency has to be greater than  $2f_m$ . Which is equivalent to assert that the sampling frequency  $F_s$  must be greater than, or equal to, twice the highest frequency detected (valid for signals with

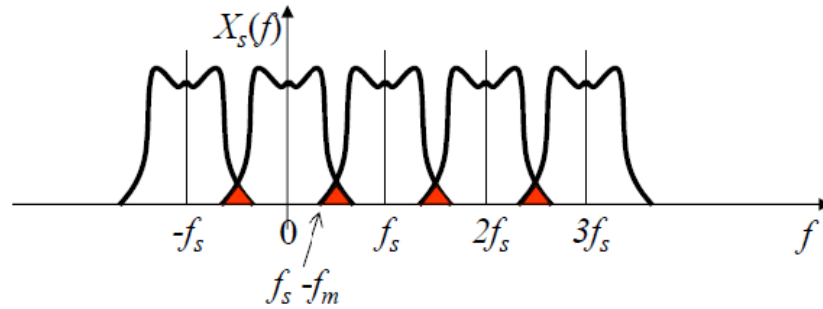


Figure 4.11: Signal spectrum which does not respect Nyquist condition

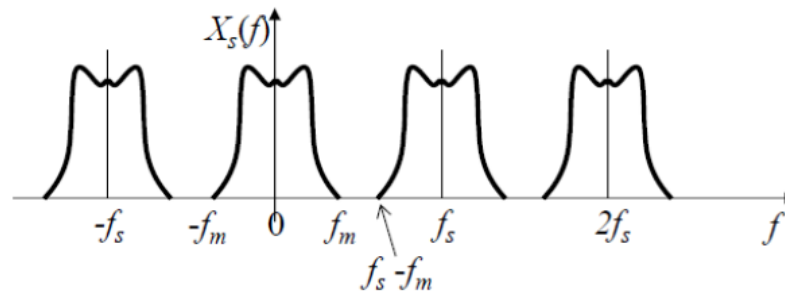


Figure 4.12: Sampling frequency impulses

limited bandwidth), a condition known as Nyquist condition. If it is violated, frequency components greater than half the sampling frequency are incorrectly identified as frequency components below half the sampling frequency, thus resulting in a wrong signal representation (fig. 4.11).

$$f_s = \frac{1}{T_s} \geq 2f_m \tag{4.14}$$

Anyway, it is common in order to avoid aliasing phenomena to pre-process the analogue signal using an anti-aliasing filter with a cutoff frequency equal to  $F_s/2$  before passing to the analogue-to-digital converter, as shown in figure 4.13. The filter is a lowpass which abates frequencies greater than the Nyquist limit in order to assure the observation of the homonymous condition. Obviously, this filter has a transient band of frequency not properly filtered, causing the maximum frequency to shift to :

$$f_m = \frac{F_s}{2.56} \tag{4.15}$$

to include the effect of the transient band [2]. Which means that a sinusoidal signal requires at least 2.56 samples in order not to suffer of aliasing. Supposing that the data

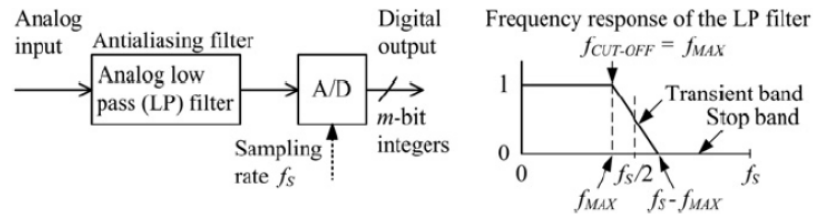


Figure 4.13: Anti-aliasing filter

are not filtered using an anti-aliasing filter, Nyquist condition affects the highest frequency detectable rather than the sampling frequency.

If Nyquist condition is not respected, aliasing occurs, with an effect as the one shown in figure 4.14.

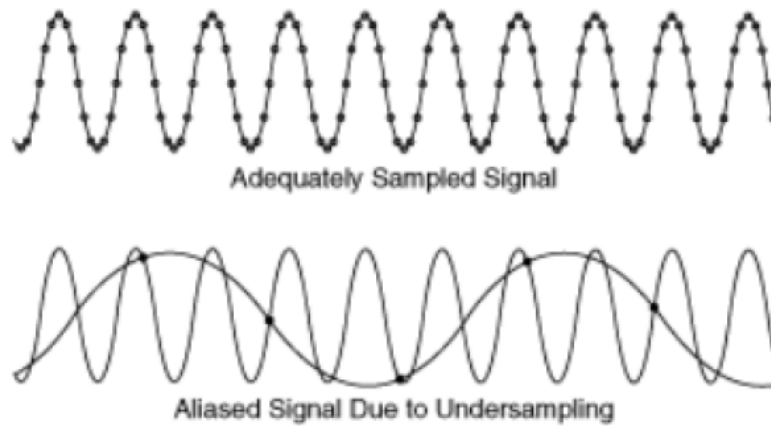


Figure 4.14: Aliasing effect

### 4.2.2 Truncation and Windowing

Considering a real sampling process, the number of samplings will be finite and with a certain extension in the time domain. Despite the signal being finite, DFT algorithms require the input signal to be divided into a discrete number of intervals, both for stationary and non-stationary signals. In order to do so, the signal is truncated at fixed time moments, and the time between two of them is called windowing period, a fundamental analysis parameter.

However, this division into several segments causes the rise of the aforementioned error called spectral leakage. In fact, the DFT algorithm assumes that the signal record is periodic over time with a period equal to the windowing time. If the signal segment has

not an integer number of cycles within the windowing period, spectral leakage occurs. This phenomenon causes energy to be spread over a frequency band, instead of entirely assign it to the correct one. Every frequency spectrum suffers for spectral leakage, up to a certain point; there are only two cases that completely avoid it: the first case is if a sampling synchronous with the signal is performed, a condition that guarantees the number of cycles to be integral. The second case is if the user captures a transient signal that fits entirely in the time interval. In real-life cases, however, the signal to be analyzed is unknown and can be assumed stationary with respect to the time segment, that is to say, that the signal is present before and after the sampling, and cannot be considered transient with respect to the windowing period. As a consequence, in real cases, it is impossible to completely avoid spectral leakage.

However, it is possible to dramatically reduce its influence by applying a windowing function to the truncated signal.

A generic windowing function  $w(t)$  is a time-dependent function which multiplies the signal segment in the time domain:

$$x_w(t) = x(t) \cdot w(t) \quad (4.16)$$

Whereas in the frequency domain, to apply a windowing function means to calculate the convolution between the signal transform  $X(f)$  and the windowing function transform  $W(f)$ :

$$X_w(f) = X(f) * W(f) \quad (4.17)$$

Actually, applying no windowing function, it is equivalent to multiply the signal for a rectangular window, defined as:

$$w(t) = \begin{cases} 1 & \text{for } -\frac{T}{2} \leq t \leq \frac{T}{2} \\ 0 & \text{elsewhere} \end{cases} \quad (4.18)$$

Obviously, the rectangular window does not influence spectral leakage, so other functions are used such as Hanning, Hamming, Blackman and FlatTop shown in figure 4.15, which abate the error by progressively erasing the signal when moving from the center of the window to its delimiters. The result is that the central part of the window is the one that contributes the most to the signal. For the following frequency analysis, it is important to keep in mind that it is not possible to be precise both in frequency and amplitude, a compromise has to be reached, using specific windowing functions (Hanning) or, according to the analysis to perform, to privilege either amplitude or frequency.

The continuous windowing function  $w(t)$  need to be discretized too in order to be applied

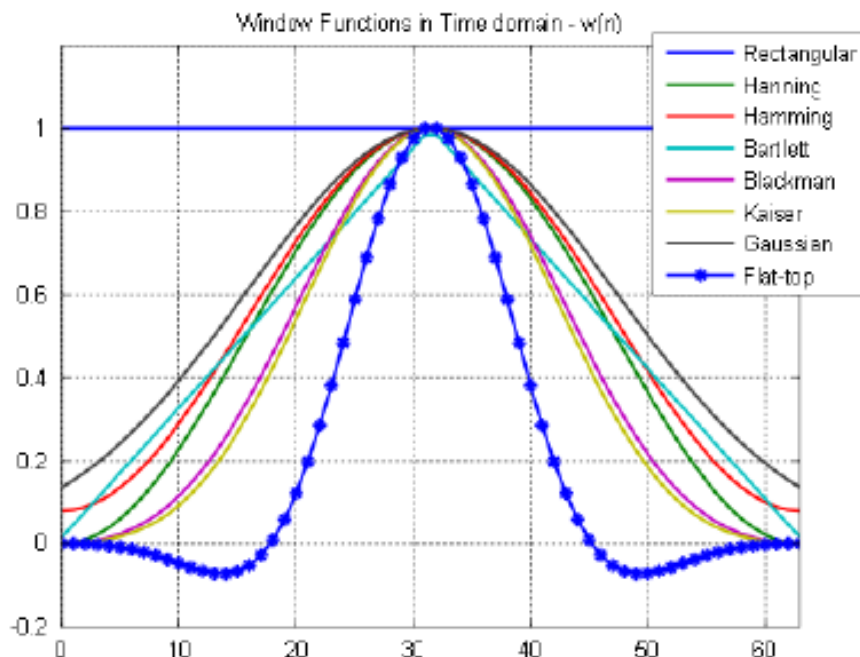


Figure 4.15: Windowing functions [7]

to the signal, in the same interval  $T = 1/F_s$  between two values identified by the sampling frequency  $F_s$ . Therefore, the function becomes dependent only on the  $N$  points that discretize the window.

Furthermore, it is necessary to multiply the signal segment by a coherent gain (depending on the windowing function chosen) in order to depict the correct frequency spectrum amplitude:

$$w(n) = \frac{w^*(n)}{\text{CoherentGain}} \quad (4.19)$$

In order to better understand the role of the windowing function in enhancing the spectrum precision, let us introduce an example. In figure 4.16 is showed an example of the application of a windowing function to a 5 Hz sine signal with an amplitude of 2,  $F_s = 1000\text{Hz}$ , and a windowing period of 1.5 sec [7]. In the middle figure, in red is showed the windowing function (Hanning) and in blue the product  $x(t) \cdot w(t)$  result of its application to the signal. As we can see in the rightmost plot, to apply the windowing function to the signal causes the frequency spectrum to be more precise. In fact, ideally, it should identify a single frequency (5 Hz); instead, a range of frequency is included, meaning that energy is incorrectly spread. A reduction of this error is obtained with a windowing function, which causes the frequency range to narrow to  $\Delta f = 1/T_w = 2/3 = 0.66\text{ Hz}$ , with

a consequent increase in amplitude precision, closer to the actual value of 2. Let us now

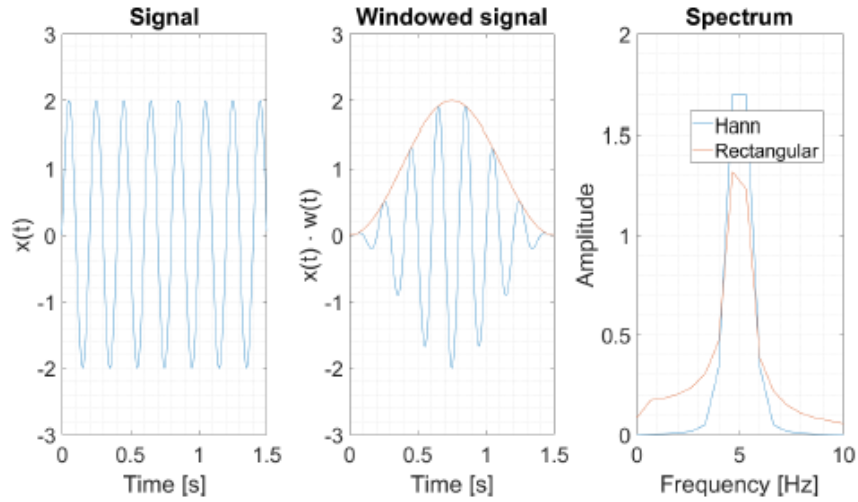


Figure 4.16: Windowed 5 Hz sine signal and its spectrum with  $\Delta f = 2/3 Hz$  [7]

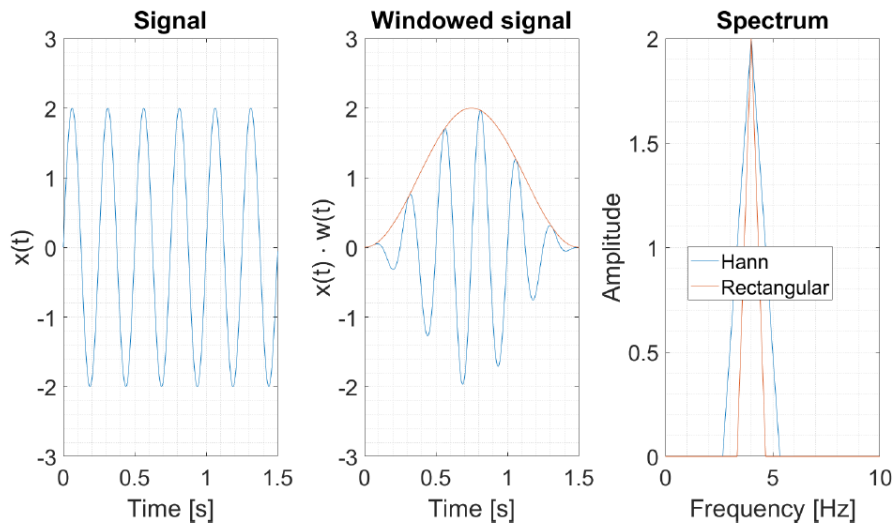


Figure 4.17: Windowed 4 Hz sine signal and its spectrum with  $\Delta f = 2/3 Hz$  [7]

consider another signal, shown in figure 4.17 in order to highlight the influence of having a signal periodic over the windowing period. Indeed, in the previous case, in the windowing period, there wasn't an integer amount of cycles:  $5 Hz \cdot 1.5 s = 7.5$ . Therefore, we can, for example, consider a signal with a frequency of 4 Hz, thus an integer number of cycles over the windowing period  $4 \cdot 1.5 = 6$ , thus truncation does not introduce spectral leakage. In this case, as shown in figure 4.17, the amplitude precision is guaranteed, whereas the

optimal prediction in frequency is given by the rectangular window, in fact, reducing the amplitude of the signal itself causes a minimal spectral leakage, which is the reason why the best solution (with very slight differences) seems not to apply a windowing function. But this result is true only if the windowing period contains an integer number of cycles, which is a very restricted case. That's the reason why windowing functions are always used because they guarantee a far more precise result in case spectral leakage is caused, and a slightly worst one in case it is not.

As aforementioned, there are several types of windowing functions, which offers solutions to privilege either frequency precision (rectangular, Hanning and Hamming) or amplitude one (FlatTop), and also some optimum solutions, the trade-off has to be carried on considering the aim of each analysis. More information about windowing function can be found in literature, such as [9] and [14].

In order not to lose information in the side portions of a windowed signal, it is required to overlap the different segments (fig. 4.18).

Furthermore, in the example presented up to this point, the frequency of the signal is

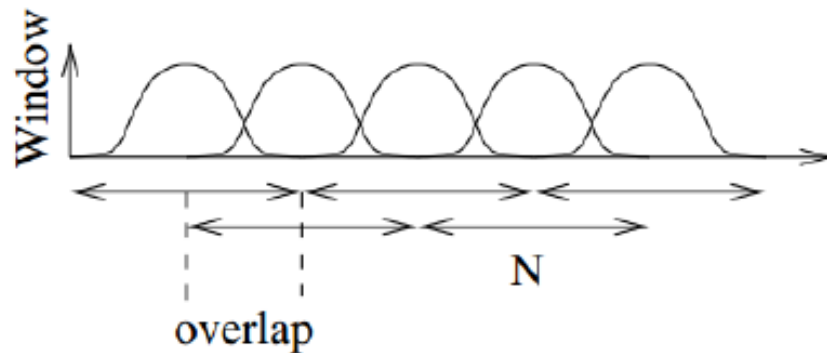


Figure 4.18: Overlapped signal [7]

assumed to be constant, whereas in a real case, in which the signal is non-stationary, it is necessary to portion the signal into windows that allow keeping guaranteed the hypothesis of stationarity in order to correctly compute the FFT. The overlap is a further method to reduce the frequency variation, but as a counter effect increases by far the computational cost. Obviously, the higher the overlap, the more precise the analysis would be, but for each windowing function, an optimum overlap percentage is given, which is the best solution in terms of the computational cost and signal quality.

### 4.2.3 Frequency discretization

The result of the FFT is a discrete frequency spectrum, not a continuous function, which therefore by definition does not describe the entire range of frequencies between the minimum and the maximum considered. It gives a result discretized in so-called bins, which inevitably generates the picket fence effect showed in figure 4.19. In the figure, the

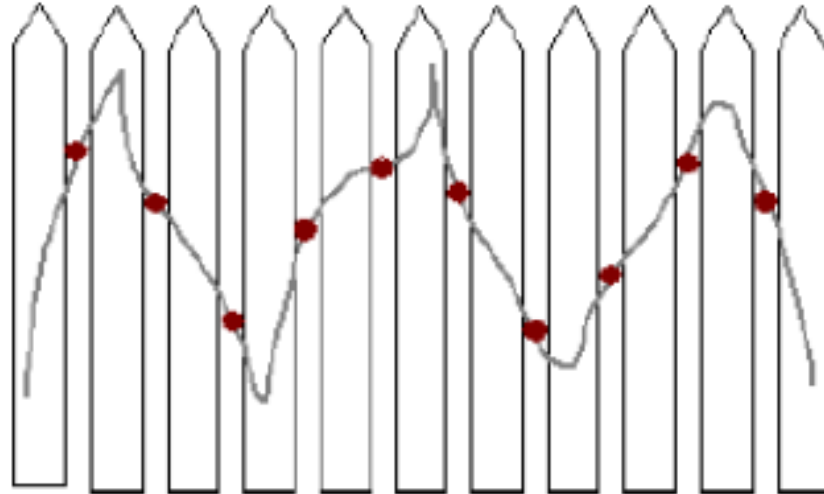


Figure 4.19: Visual representation of the picket fence effect [7]

dots represent the plotted spectrum value, while the lines show the continuous frequency spectrum of the signal. It is clear that discretize the signal introduces some errors, for example, if a frequency lies exactly between two bins the energy is spread between both the bins and this explains why an inaccurate value of the amplitude is obtained and the spectral leakage occurs. The signal is discretized in frequency values multiple of the frequency resolution  $\Delta_f$ , therefore, if for example a relevant peak is located outside the discretized frequencies, both an error in amplitude and a frequency shift is obtained. However, the biggest error possible occurs if no windowing function is used, and generally speaking, the error is proportional to distance in frequency between the frequency to represent and the two closest bins.

More in-depth, this error is a function of 4 parameters shown in figure 4.20:

- $\Delta dB$  is the amplitude difference between the two highest peaks adjacent to the maximum, or in other words, the distance between the real frequency and the two closest bins. So, for instance,  $\Delta dB = 0$  means that the neighbouring bins have equally shared the energy contained by a peak located in the exact middle of the two bins. Therefore, the higher the  $\Delta dB$ , the lower the probability that a frequency

is spreading energy among several bins.

- $\Delta L$  represents the amplitude difference between the real maximum and the one obtained by the FFT.
- $\Delta f$  represents the distance between the real frequency and the closest bin.
- $f_0$  is the frequency resolution

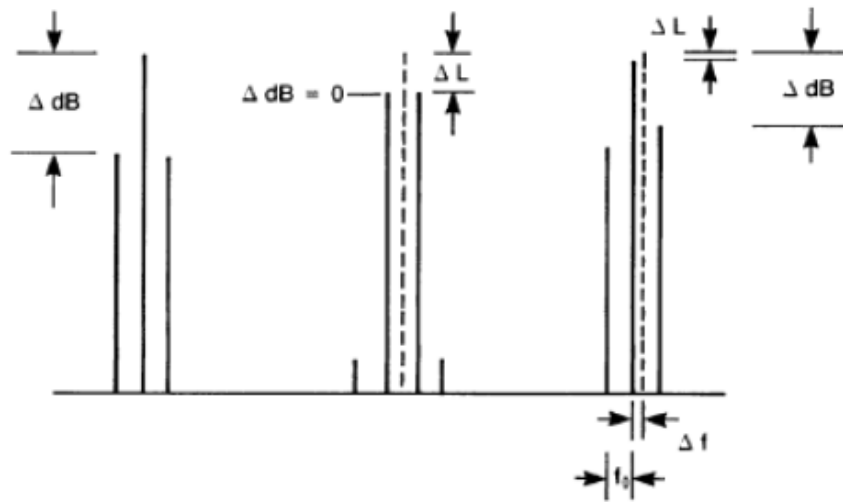


Figure 4.20: Picket fence effect errors of different windows [7]

In figure 4.21 are plotted the various windows errors caused by picket fence effect concerning frequency ( $\Delta f/f_0$ ) and amplitude ( $\Delta L$ ). The errors are plotted with respect to the  $\Delta dB$  and, as aforementioned, the highest possible error occurs when the frequency to represent lies exactly in between the two closest bin ( $\Delta dB = 0$ ), and when no windowing function is used (rectangular one). Regarding the FlatTop window, it displays a very low error both in amplitude and frequency for nearly any value of  $\Delta dB$ , which means that high precision is guaranteed but with a frequency spectrum that shows similar values on adjacent bins. This means that using the FlatTop does not guarantee to correctly identify the frequency of interest, because it is less distinguishable.

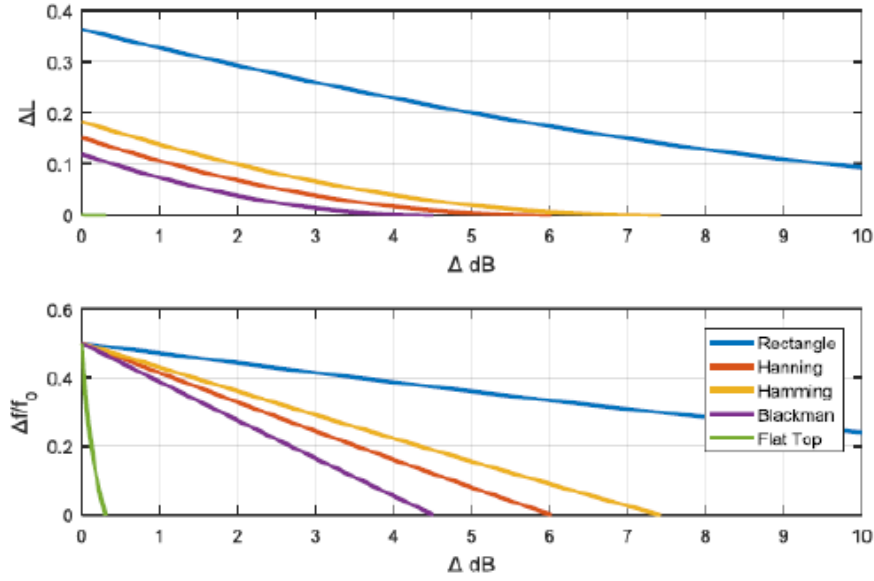


Figure 4.21: Picket fence effect errors of different windows [7]

As stated in [14], to perform a successful analysis some parameters have to be set which are directly related to each other:

- windows frequency  $f_0 = \frac{1}{T}$
- sampling frequency  $F_s = Nf_0$
- windowing period  $T = NT_0$
- sampling period of time  $T_0 = \frac{1}{F_s}$
- number of samples in a window  $N = \frac{T}{T_0}$

As shown in the correlation above, these parameters are interdependent, and it is enough to set two of them to derive all the others. Generally, the sampling frequency is fixed at a given test run, which means that the parameter to control is the windowing period  $T$ , depending on the frequency resolution that is required by the user. As a matter of fact, having a short windowing period allows for the signal segments to be considered quasi-stationary, resulting in a low amplitude error, but considering that the frequency resolution is defined as follows:

$$\Delta f = \frac{1}{T} = \frac{1}{NT_0} = \frac{F_s}{N} \quad (4.20)$$

a small windowing period will cause a rise of the picket fence error due to a large  $\Delta f$ . After all these considerations, we have understood that there is not a universal right choice, but all the parameters of frequency analysis have to be chosen to meet the needs of the user and to adapt to the feature of the signal to be analyzed.

## Chapter 5

# Code Architecture

The aim of this work has been to write a MATLAB code able to perform both frequency and order analysis, and to specialize it in order to allow the integration with existing visualization tools, besides make its usage more user friendly by developing a GUI (Graphic User Interface). In figure 5.1 the process followed by the code when a frequency analysis is performed is shown. In this given scheme, the right branch represents the automatic

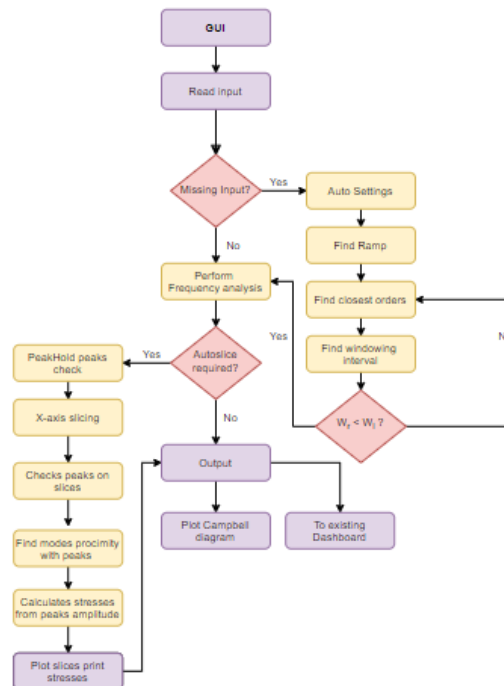


Figure 5.1: Frequency analysis workflow [7]

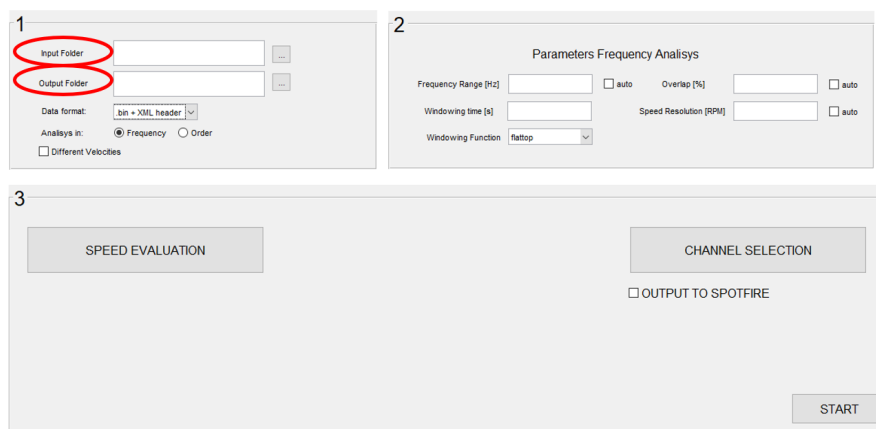
choice of parameters necessary for the frequency analysis. The block "Perform Frequency

analysis" includes the aforementioned steps varying from signal truncation to the actual perform of the Fast Fourier Transform.

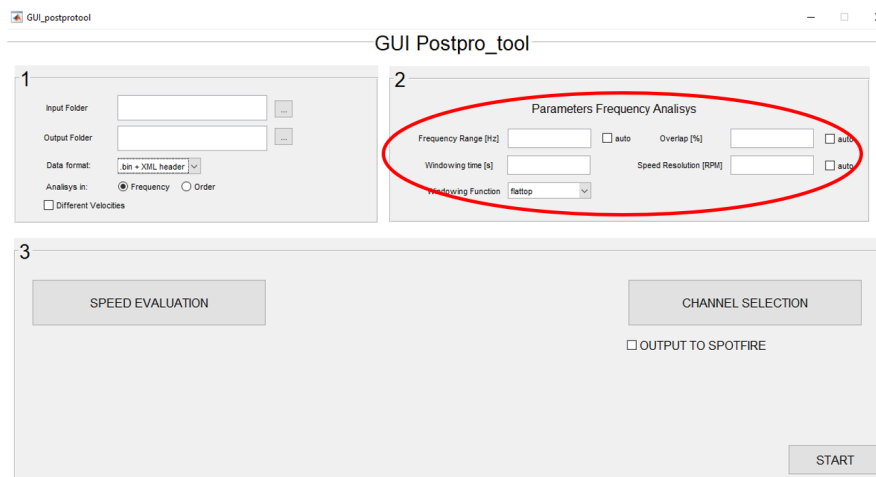
## 5.1 Code Input

Regarding the "Read Input" block, it refers to the input given by the user through the GUI:

- Input and Output directories



- Frequency analysis parameters, which on turn can be automatically chosen



- Information regarding test type

Given this information the GUI automatically run a dedicated part of the code which extracts various information from the raw data depending on the test type and on data format. For example, considering a common frequency analysis test, the velocity of the Test Article is varied in order to excite a set of frequencies to analyze the dynamic response of the structure. Therefore, the code automatically recognizes the channels dedicated to rotational speed acquisition and process them isolated, by plotting them the user is then asked to identify a velocity ramp, in order to cut the acquisition data to a specific interval of interest as shown in figure 5.2: In this specific case, two velocities of

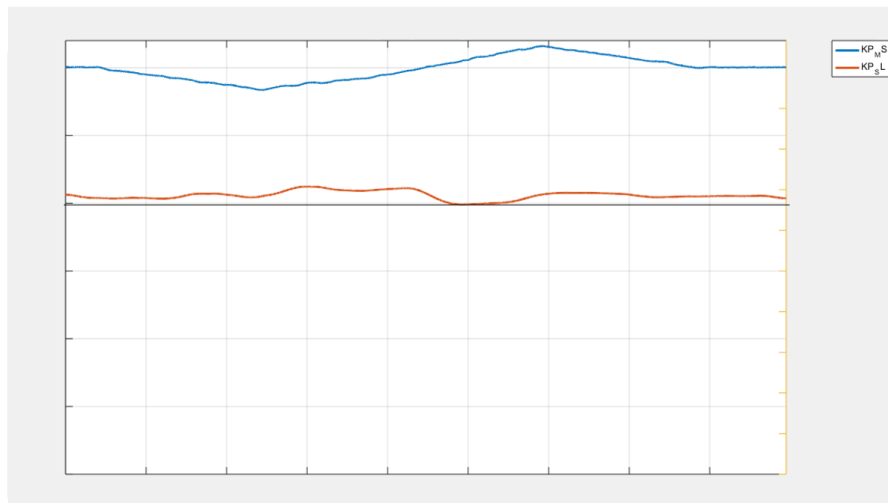
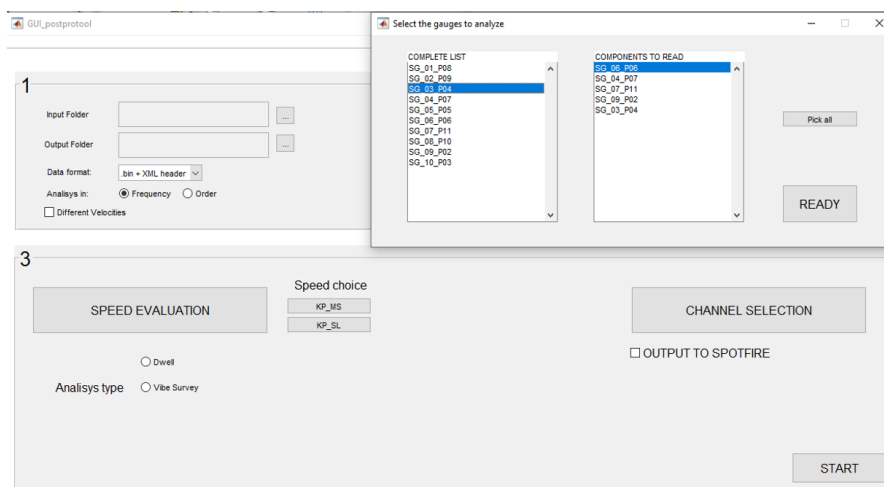


**Figure 5.2: Velocity ramp selection**

interest are identified, because in this particular test there are two shafts, one representing a magnet carrier which is the exciter, and the other the LPT disk which is the test article. In order to correctly perform the frequency analysis, the velocity of both has to be taken into consideration.

Furthermore, the code allows to pick the acquisition channels of interest, by automatically gathering them into a table, as shown in the following figure:



Such a solution is implemented in order to avoid waste of computational time to get data just from a certain Strain gauge of interest.

## 5.2 Code Output

In figure 5.1 the last blocks are dedicated to the output of the analysis. It is split into two blocks, "Plot Campbell diagram" and "To existing dashboard", which will be explained in the following section.

As aforementioned, the frequency analysis' output is the frequency spectrum of the signal, which represents energy distribution over frequencies of the signal. Up to Nyquist frequency, equal to  $F_s/2.56$ , the frequency spectrum will be accurate, above the results will be subjected to aliasing effect.

The output of the analysis consists of the frequency spectrum as a function of time or rotational speed of the shaft. This means that a 3D representation is required since the frequency spectrum is an amplitude vs frequency plot, and it has to be analyzed at vary time instants. The result of such a plot is called colourmap (figure 5.3), in such a way that is given a colour scale to the third dimension (vibration amplitude). The matrix is a  $N \times M$  where  $N$  is the number of elements in which the frequency axis is discretized, which is related to the windowing period chosen as previously explained, whereas the x-axis depends on Sampling Frequency.

Right of the colourmap, the so-called peak-hold is plotted, which represents the maximum amplitude at each frequency, whereas in the graph below the maximum amplitude for each element of the x-axis is plotted. More in-depth, the extraction of a given engine

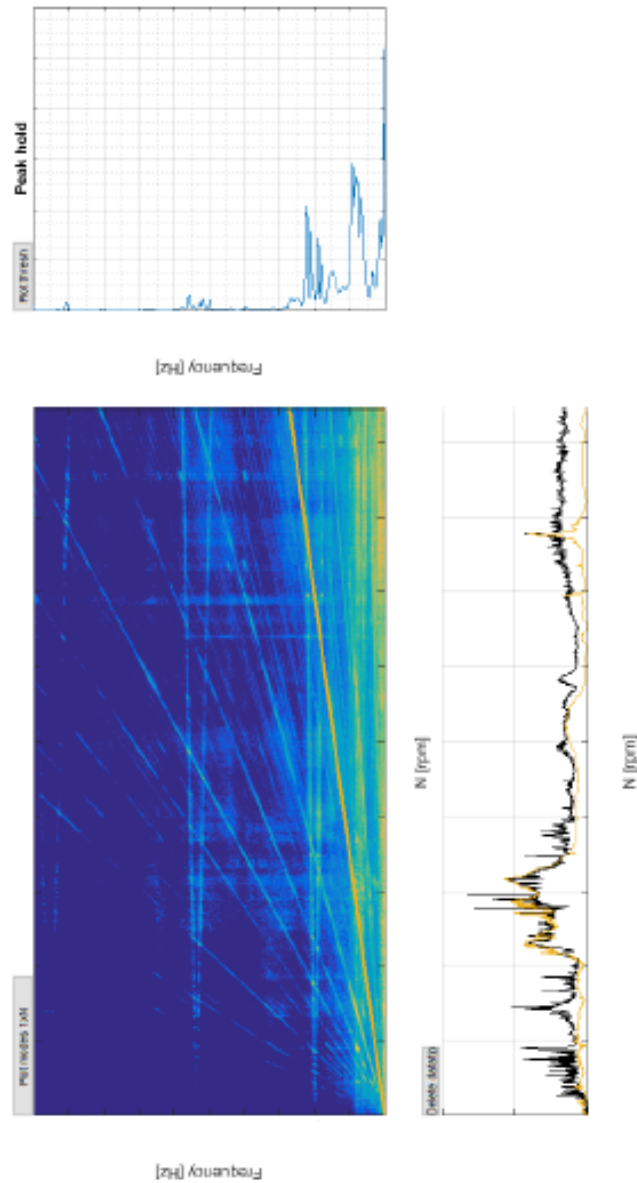


Figure 5.3: Colormap with x-axis rotational speed [7]

order is plotted in yellow, which is possible using the legend callback, that isolates a specific order, with respect to the overall signal plotted in black. This information gives the opportunity to identify the relevance of a certain event in the overall amplitude, which is particularly useful when considering gearboxes, where the transmission ratios between shafts are known, and to highlight a specific order means to verify whether an event is the main amplitude contributor of the signal acquired.

Other callbacks are active in the figure produced, generally related to zooming and panning, and among all of them, the one more used during the raw data analysis was the one associated to the "Peak Snap" button located on top of the peak-hold plot. The callback meant to update peak-hold data based on zoom in combination with this function, allow the user to isolate a specific peak of interest among the various showed in the colourmap. Furthermore, a detrending function is associated with this command, which allows eliminating noise from the signal following a procedure that will be further explained later. In figure 5.4 we can see the Output of the function described: Up to now, the description of

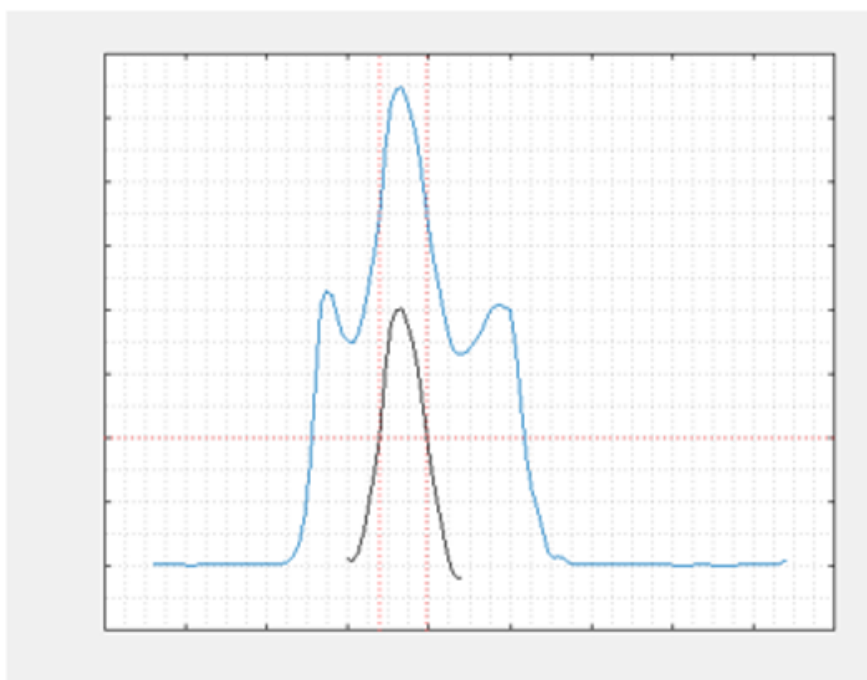


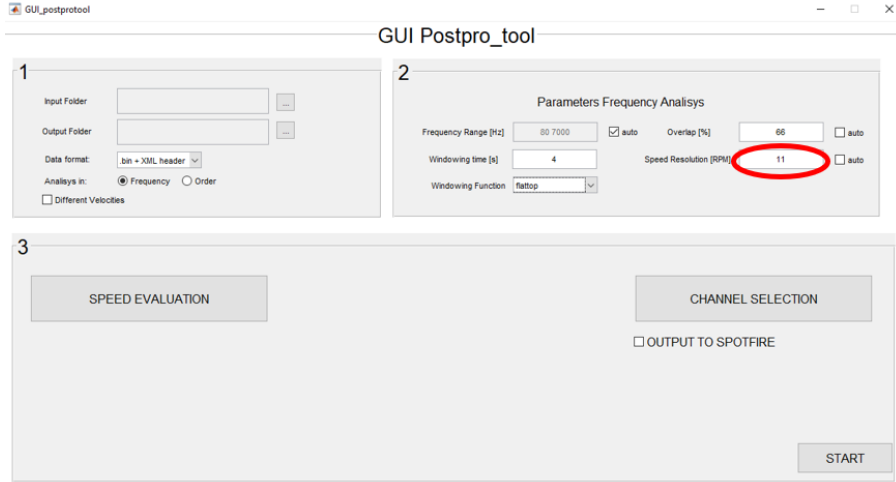
Figure 5.4: Peak isolated with the Peak snap function and its detrended signal

the "Plot Campbell" part of the block diagram has been explained, from now the section dedicated to the integration with an existing dashboard starts, showing some differences in the output produced, and some solutions that were implemented in the code.

The production of a colourmap using the default MATLAB function rises some graphical limits, in fact, both x and y-axis have to be evenly spaced. This is a relevant constraint, which acts mainly on the x-axis (considering that the y-axis is evenly spaced once that the windowing period is chosen and kept constant) when the Campbell diagram is not plotted with respect to time but to rotational speed. In fact, once the windowing period  $T_W$  is chosen, the speed x-axis spacing depends on shaft acceleration, and the spacing is given by the difference between the mean speed value in a certain window and the one

obtained in the following, which is certainly not constant. Therefore before passing the data to this MATLAB function, there is the need for modifying the output to generate an evenly spaced speed x-axis in order to avoid errors generation.

There are substantially two ways to obtain an evenly spaced x-axis. The first one is to define a fixed x-axis resolution, which is possible by specifying a value in the GUI's corresponding box: In this case after having collected all the frequency spectra coherently



with the  $T_W$  chosen, a contraction of the result is obtained by considering a certain speed value  $x_{int}$ , which is an integer multiple of the speed resolution chosen, and selecting the maximum value of amplitude for each frequency contained in all the frequency spectra in the interval between  $x_{int} - \frac{x_{axis\ resolution}}{2}$  and  $x_{int} + \frac{x_{axis\ resolution}}{2}$ .

The second way is to stretch the matrix obtained, by considering the smallest spacing in the x-axis vector, which corresponds to the lowest acceleration phase and to generate a new x-axis with that spacing. The new frequency spectra introduced by this process are filled by duplicating the adjacent ones, as shown in figure ??:

In particular, it is clearly introduced an error by following this practice connected with the relative position of the elements of the two vectors and with the  $dx$ .

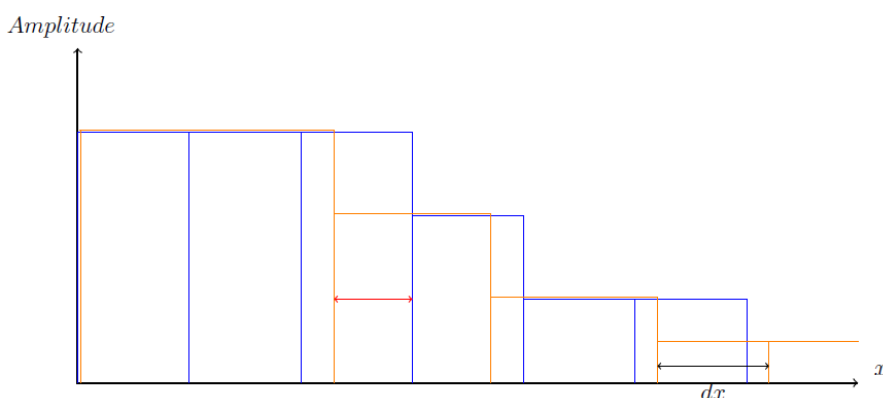


**Figure 5.5:** In green the original unevenly spaced x-axis vector, in blue the new evenly spaced one. In red the error introduced by this procedure

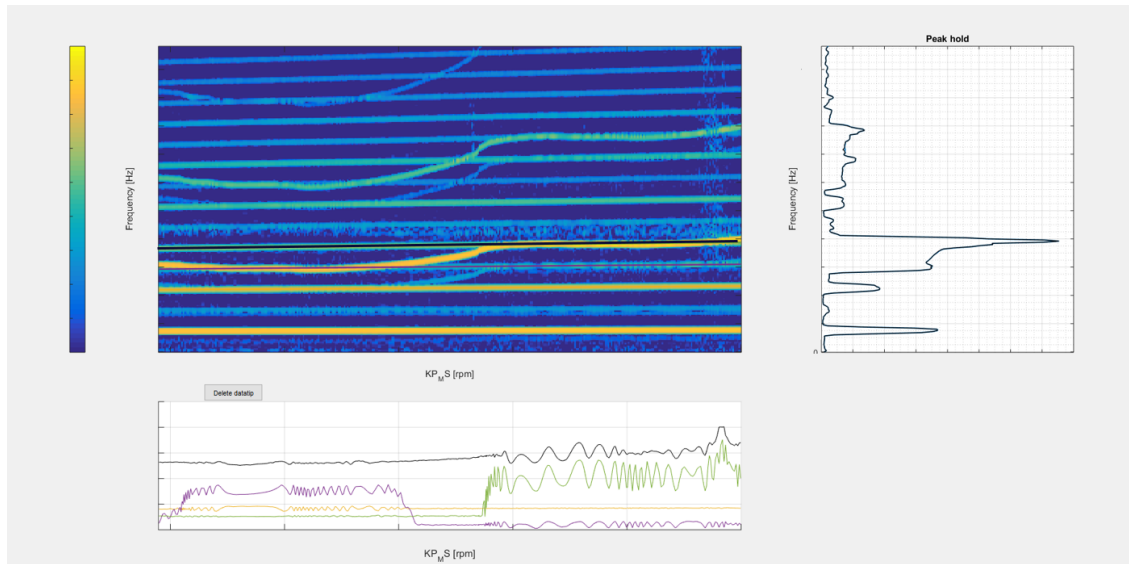
These problems are related to the traditional output of the tool, which is, as mentioned, a graphical output.

A different approach is followed in the other output block the "To existing Dashboard" where there are some advantages because the result is a numerical matrix, which is then graphically interpreted by an external tool. This approach allows avoiding problem connected with the aforementioned MATLAB function that creates the colourmap, the graphical stretch of the matrix or its contraction is not necessary anymore. Actually, the objective of the integration was to substitute a black-box post-processing tool, with a customizable product, and to abate the computational cost of the post-processing, following a benchmarking activity.

Each colourmap is a matrix  $N \times M$  with a number of elements completely identified by the windowing time  $T_W$  (which influences both the frequency resolution and the x-axis resolution), given that the speed-axis resolution is not forced with the command previously described of the GUI. In order to reduce the computational cost, some actions are required, and a selection of data is desirable. As a matter of fact, hundreds of sensors are exploited in a testing activity, and each of them would have given in output a colourmap, which consists of a numerical matrix with  $10^6$  elements on average. The selection of data was made through substantially four steps:

- A dynamic threshold which eliminates the results not of interest in terms of vibration amplitude
- An x-axis speed resolution fixed in order to reduce the number of columns of the matrix
- For each frequency, a reduced number of values is considered in order to guarantee

a non-oscillating frequency spectrum. Therefore considering the following figure, the approach employed in the rightmost plot is followed even if multiple peaks are identified in the plot below.



- A frequency resolution variable with the y-axis is guaranteed, considering that the precision required is a function of the absolute frequency value, and therefore it is not necessary to have a fixed high resolution for all the frequency interval. In order to obtain such a result, the FFT is performed multiple times with variable windowing period, and the resulting matrices combined to give the following result:

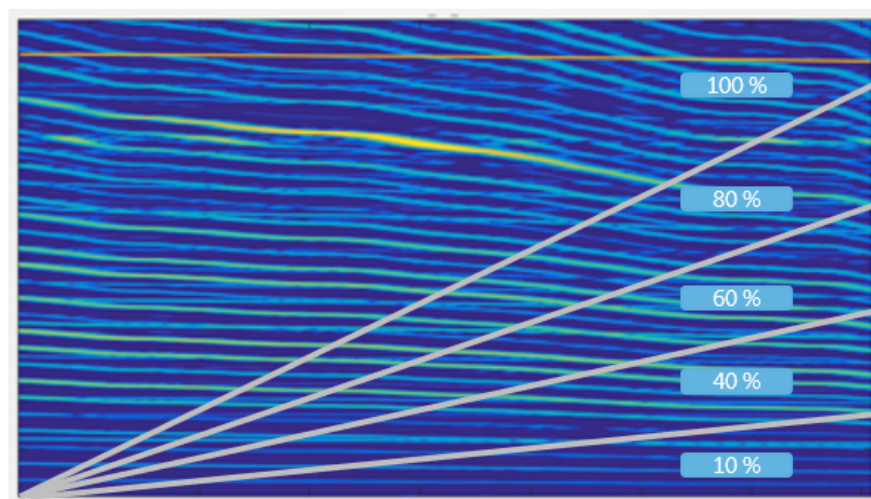


Figure 5.6: Frequency resolution variable along y-axis

By applying all these methods together, it was possible to reduce the computational time of the 80 % with respect to the previous tool exploited.

## Chapter 6

# Tool Applications

The code described up to this point was applied to an innovative test, using a traditional acquisition system based on Strain Gauges and a more innovative one the BTT (Blade Tip Timing). A comparison of the results is then considered showing, which is the optimal acquisition system for the validation of the technology of interest.

### 6.1 The Spinning Test Rig

In this section, an introduction to the typology of the testing method is given by describing the Test Rig developed by Politecnico di Torino in collaboration with *GE Avio Aero* [3], which exhaustively represents the test analyzed during this thesis work.

The experimental campaign was carried out onto two dummy disks. Where one has the simple geometry of a flat plate, and it is characterized by bending vibration modes of the blades in the disk axial direction, whereas the second one was designed in order to simulate a dynamic behaviour closer to that of a real turbine disk, interconnected at the tip by an outer ring.

Regarding the testing conditions, these disks were tested in a laboratory spinning rig at room temperature under vacuum conditions [5]. As shown in figure 6.1 a) the test rig has a vertical axis with two cylindrical protective structures (1 and 2) coaxial to the rotating shaft that is positioned under the floor. At the top of the shaft a flange allows the disk accommodation 3). The cylinder one also supports two static rings (figure 6.1 b)): the ring 1 keeps in a fixed position a set of permanent magnets that are used to excite the rotating disk, while the ring 2 holds the BTT laser sensors.

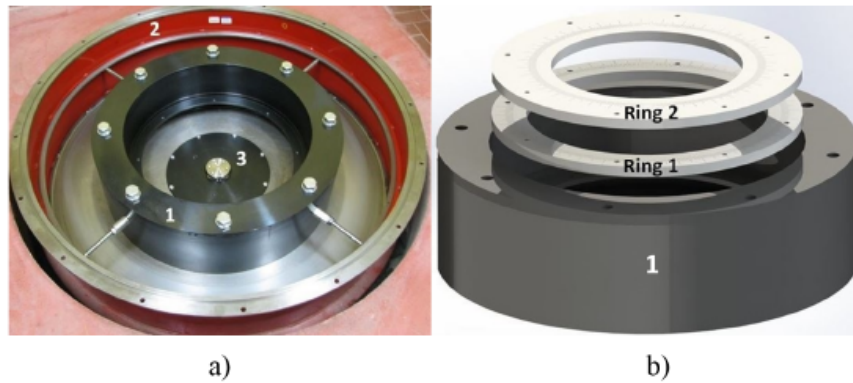


**Figure 6.1: The spinning rig a) and the supporting rings for the magnets and laser sensors positioning b) [3]**

### 6.1.1 The Dummy Disks

The dummy disk (figure 6.2) is an aluminium disk with a flat plate geometry where each blade can be approximated with a cantilever beam. The dummy disk 1 has 12 identical blades whose length and width are 150 mm and 25 mm respectively. The thickness and the outer diameter of the disk are 5 mm and 400 mm. A cylindrical magnet with a 5 mm diameter and 5 mm height is glued in a housing drilled at the tip of each blade.

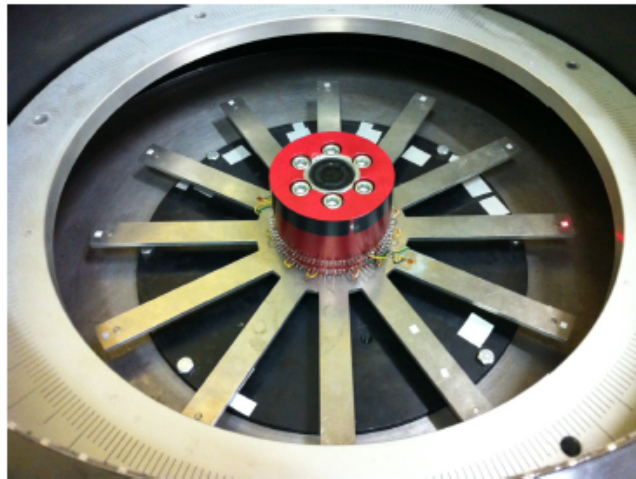


**Figure 6.2: The dummy disk 1 within the spinning test rig [3]**

The dummy disk 2 (figure 6.3) was designed to have a dynamic behaviour closer to a real turbine disk. The blades are connected to each other at the tips by an outer ring as in the case of shrouded bladed disks. It is a single piece made of the ferromagnetic steel AISI 460, in order to allow the magnetic interaction between the permanent magnets and the

blade airfoils. It has 32 real profiled blades whose length and aspect ratio are respectively 100 mm and 7.31. Its outer disk diameter and axial height are 630 mm and 20 mm.



Figure 6.3: The dummy disk 2 within the spinning test rig [3]

### 6.1.2 The Excitation System

The excitation system in the spinning test rig uses cylindrical permanent magnets (diameter 18 mm, height 10 mm, grade N52). The magnets are mounted in evenly spaced positions on the static ring facing the rotating dummy disk (the Ring 1 in figure 6.1 a)). A graduated scale impressed on the ring 1 upper surface is used to fix the magnets at the right angular positions [5].

Several supporting rings with different inner diameters are available in order to guarantee the correct radial positioning of the permanent magnets. Each magnet is glued on the tip of a screw that allows the regulation of the axial gap with respect to the disk blades (figure 6.4)

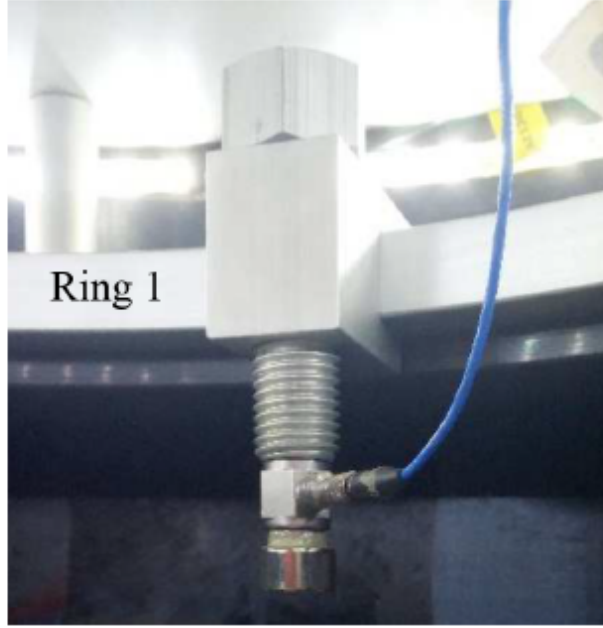


Figure 6.4: Fixed magnet and load cell exciting the rotating disk [3]

Six of the magnets were instrumented with force transducers for the measurement of the axial force exerted on the blades during the tests [5].

The number of magnets used in a specific test must be equal to the main engine order (EO) characterizing the excitation force that should be simulated. The main engine order  $EO_m$  can be defined as the first non-null harmonic index resulting from the Fourier transform of the excitation force. In general for  $m$  equally spaced magnets, the EO pattern exciting the disk is defined as follows:

$$EO_m^i = i \cdot m, \quad \forall i = 1, 2, 3, \dots \quad (6.1)$$

For example, if 3 is the number of equally spaced magnets exciting the disk, the force profile acting on each blade is that of figure 6.5 a). The harmonic content of such profile is shown in figure 6.5 b), where some EO excitation is plotted. According to the previous description, the main harmonic index is  $EO_m^1 = 3$ , while the less important harmonic contributes have EO defined as stated in Eqn. 6.1 for  $i \neq 1$ . In fact, each harmonic function may excite a mode shape having  $h$  nodal diameters and the EO is defined as follows:

$$EO = z \cdot N_s \pm h, \quad \forall z \in \mathbb{N} \quad (6.2)$$

where  $N_s$  is the number of blades and  $z$  is a positive integer.

The disk's excitation frequency  $f_{exc}$  can be calculated as:

$$f_{exc} = \frac{EO \cdot n}{60} \quad (6.3)$$

where the rotation speed  $n$  and  $f_{exc}$  are expressed respectively in RPM and Hz. From the previous equation, it can be noted that for increasing EO values the bladed disk can be excited at the same excitation frequency  $f_{exc}$  for lower values of the rotation speed  $n$ .

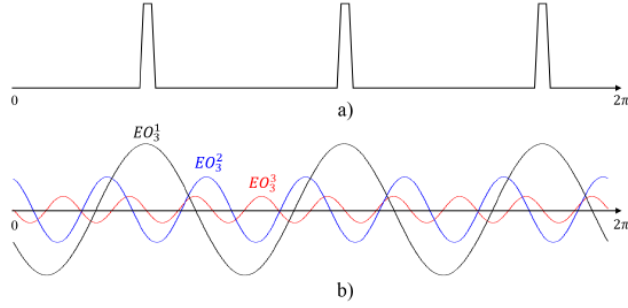


Figure 6.5: Magnetic force profile acting on each blade a) and its harmonic content b).

## 6.2 The Strain Measurement System

The strain gauge is a device used to measure strain on an object. It is basically a flexible insulating backing which supports a metallic foil pattern, which is attached to an object by a suitable adhesive. When the object is deformed, the foil is deformed, causing its electrical resistance to change, this difference is usually measured using a Wheatstone bridge, and it is possible to relate it to the strain with a quantity known as the gauge factor [17].

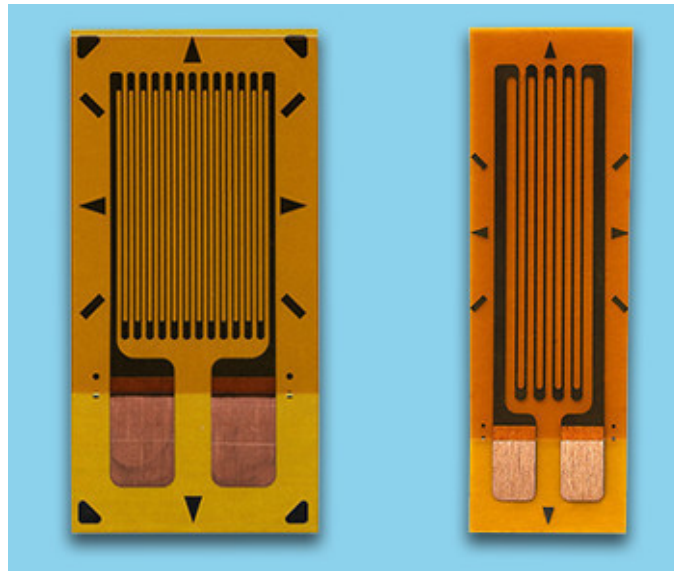


Figure 6.6: Strain gauge

The prime physical property behind this device is the electrical conductance and its dependence on the conductor's geometry. More in-depth, if a conductor is stretched within the limits of its elasticity, it will become narrower and longer, increasing its electrical resistance end-to-end. Conversely, when a conductor is compressed, its resistance decreases end-to-end. Later on, the effect on this acquisition method of magnetic disturbance will be described, and the solution adopted to overcome these problems explained, from now the description of the strain gauges application to the test rig follows.



Figure 6.7: Strain gauge at the blade root of the dummy disk 1 a), strain gauge at the back of the airfoil of a dummy disk 2 blade b) [3]

The two dummy disks were instrumented by means of strain gauges. For both the disks the identification of the strain gauge positions came out from their FE modal analysis in cyclic symmetry conditions. Areas of high strains and low strain gradients were identified as the best location for strain gauges. The strain gauges signals were acquired through a telemetry system. For the dummy disk 1 the strain gauges were attached at the two sides of the blade root (Figure 6.7 a)). This position was chosen in order to measure the Out-Of-Plane (OOP) bending mode (1F) belonging to its first modal family. The strain gauges adopted are composed by a single grid of dimension 1.52 mm x 3.05 mm, with a grid resistance of 350  $\Omega$ . The two grids at the two sides of the blade were connected together with a half-bridge. For the dummy disk 2 the strain gauge was applied on the back of a blade airfoil (Figure 6.7 b)). The selected area was not affected by strain gradients for both the flap-restricted (1FR) and the torsional (1T) mode shapes belonging to its second and third modal family respectively (figure 6.8)

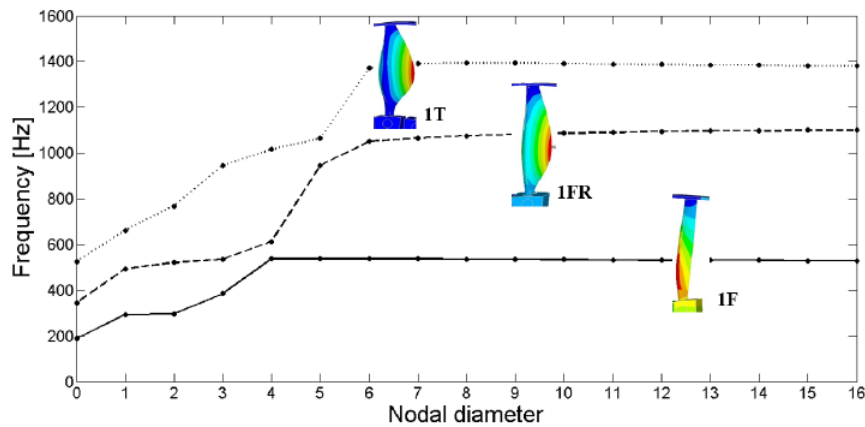
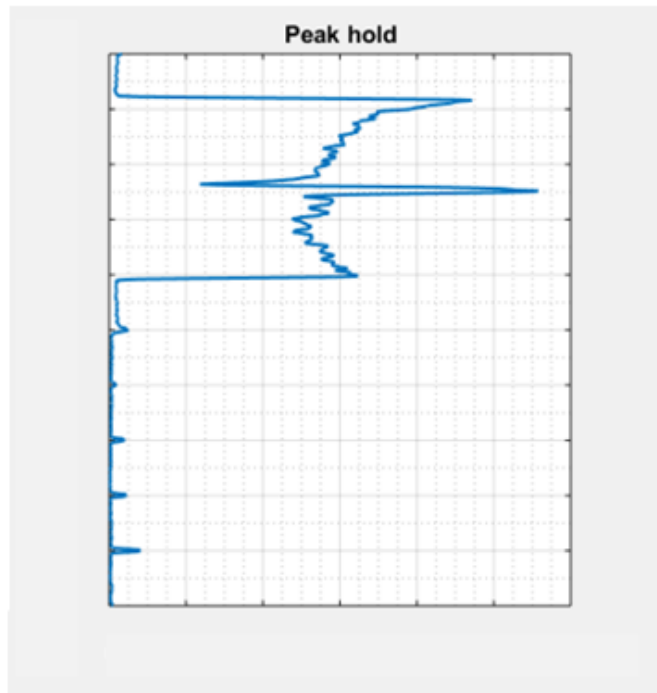


Figure 6.8: FreND diagram for the dummy disk 2 [3]

### 6.2.1 Strain Gauges Postprocessing

The code aforementioned was exploited to post-process the data acquired by the strain gauges. As stated, the test is conducted in-vacuum conditions, and the excitation method cause blades vibration thanks to a magnetic forcing, rising several adversities for this traditional acquisition method, by definition based on the measurement of a voltage variation. In this case, the rotation of the magnetic field is a function of the test article and magnet carrier rotational velocity, causing a linear offset due to magnetic disturbance as shown in figure 6.9:



**Figure 6.9: Magnetic disturbance resulting in a linear offset**

Obviously, this problem could have compromised the post-processing analysis, because it affects the vibration amplitude measured, which is up-shifted, and the Q factor estimation, which is an important indicator of blades' damping, due to a distortion of the peak shape. More in-depth, the Q factor is defined as a dimensionless parameter that describes how underdamped an oscillator or resonator is. It is calculated as the ratio between a resonator's centre of frequency to its bandwidth as shown in the following equation and in figure 6.10:

$$Q = \frac{f_0}{\Delta f} \quad (6.4)$$

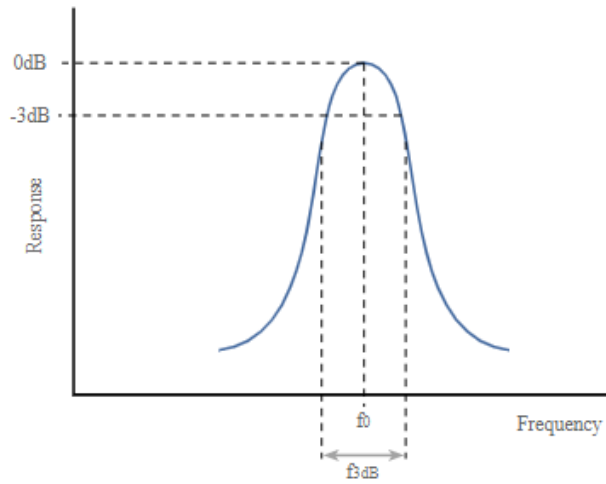


**Figure 6.10: Q factor parameters**

and it is directly connected to the damping following this relation:

$$\zeta = \frac{1}{2Q} \tag{6.5}$$

where  $\zeta$  is the damping.

It is clear that a minimal deformation of the peak would immediately affect the precision of the post-processing results. Therefore the solution that was implemented in the code was a de-trending function, that combines the isolation of the peak performed by the "Peak Snap" function described before, and performs a linear de-trending proportional to the rotational speed of the test article to eliminate the magnetic noise as shown in the following figure:

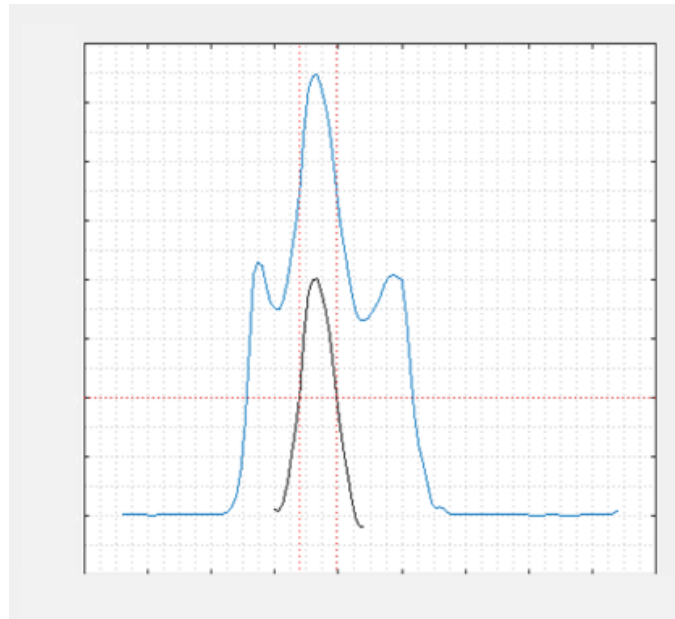
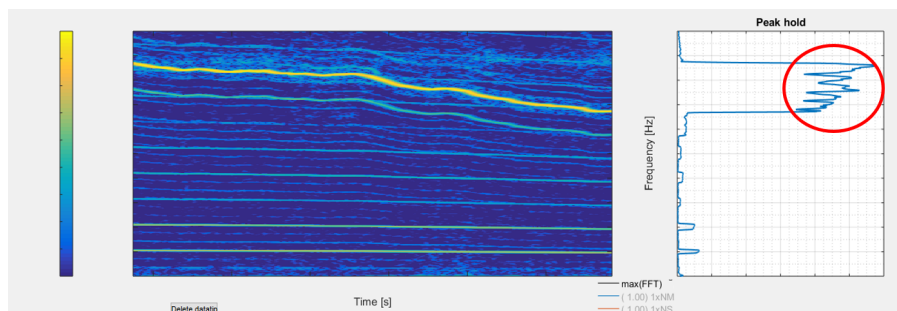


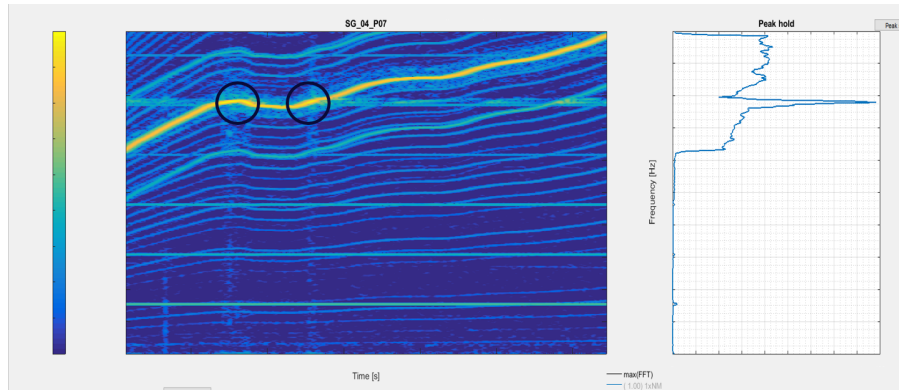
**Figure 6.11: De-trending result**

More in-depth, in figure 6.11 the blue peak is the one obtained by the "Peak Snap" function, which allows the user, by means of a cursor, to select the peak of interest from the Peak Hold of a given testing condition, in black the result of the de-trending process, which abates the magnetic offset and reduces the peak distortion. The resulting peak is theoretically more representative of the real peak shape, and the analysis in terms of vibration patterns of the disk was then conducted following this algorithm. The main concern connected to this method is that it is not automatable, it strongly depends on user's choices, for example considering the peak limits choice, in some conditions largely different result in terms of peak shape can be obtained. From now, a list of the main problems faced during the post-processing is given, in order to better understand how difficult it can be the correct identification of the peak to be de-trended:

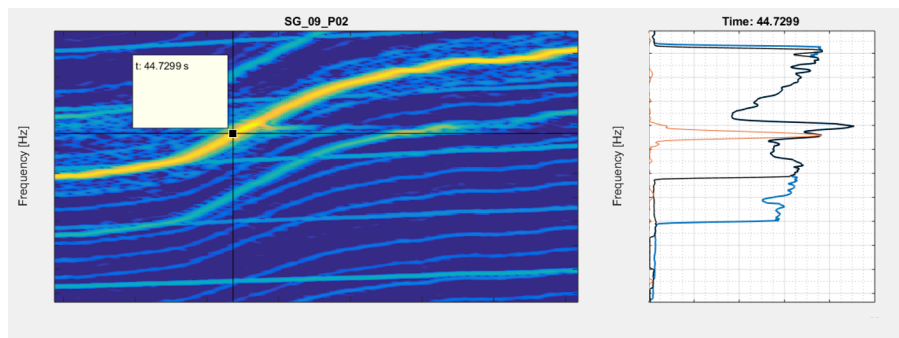
- High level of noise



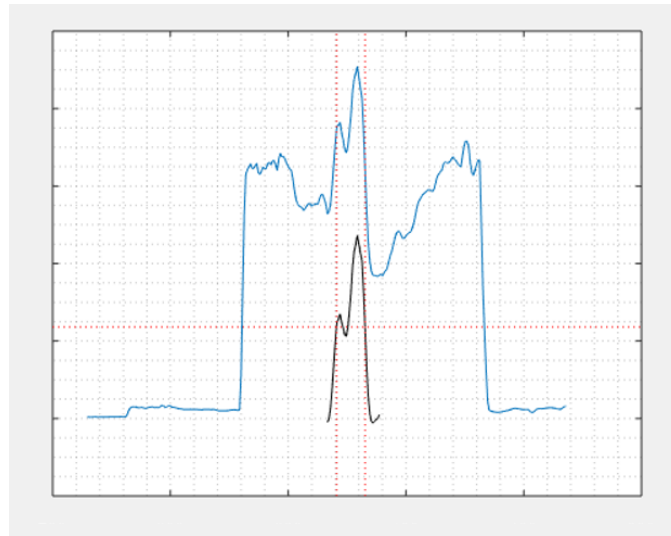
- Speed constant during resonance, in such a condition the peak hold shows just the maximum peak of the multiple occurring where speed is constant, losing the information of evolution in time of the resonance



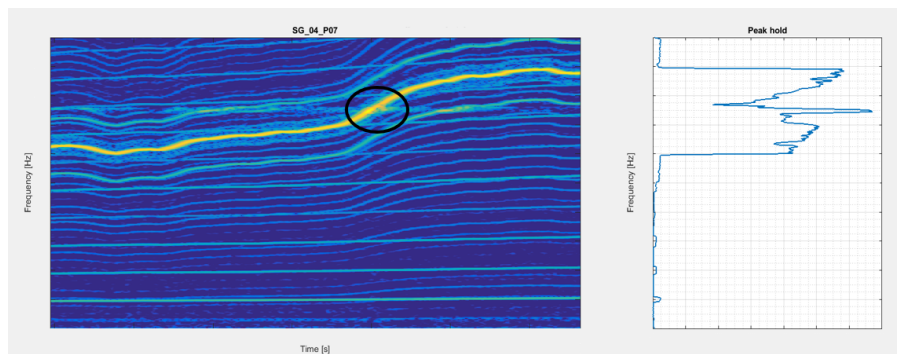
- Multiple peaks plausible for target frequency



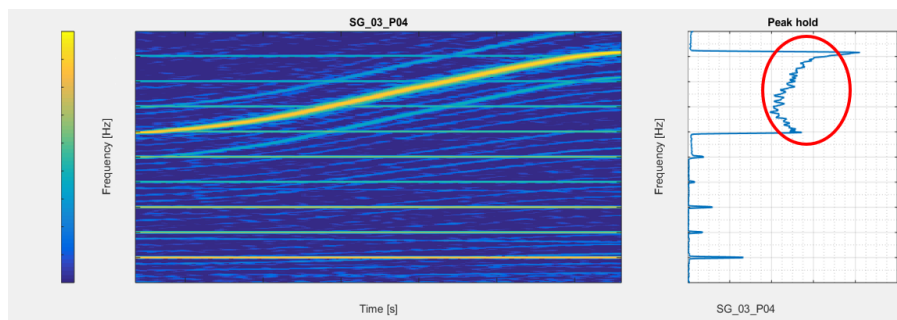
This effect showing a double peak in the frequency spectrum is particularly critical because it causes unreliability of the Q factor estimation. Various reasons could be associated to this phenomenon, for example, the oscillation of the velocity profile when close to resonance frequency or considering the analysis parameters, the choice of an incorrect windowing period, which causes the peak to split between two frequency bins.



- Negative peak which seems to abate the magnetic noise. This condition will be discussed later to better understand the variation in the results depending on peak limit's choice.



- No peak detection

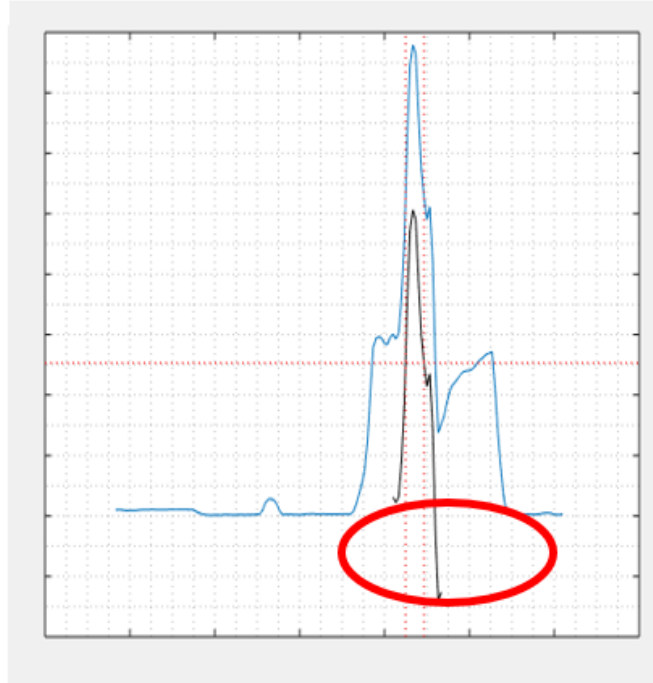


All these problems were associated with a signal quality code, in such a way to keep track of when they occur and to isolate the reliable signal from the rest. Generally speaking,

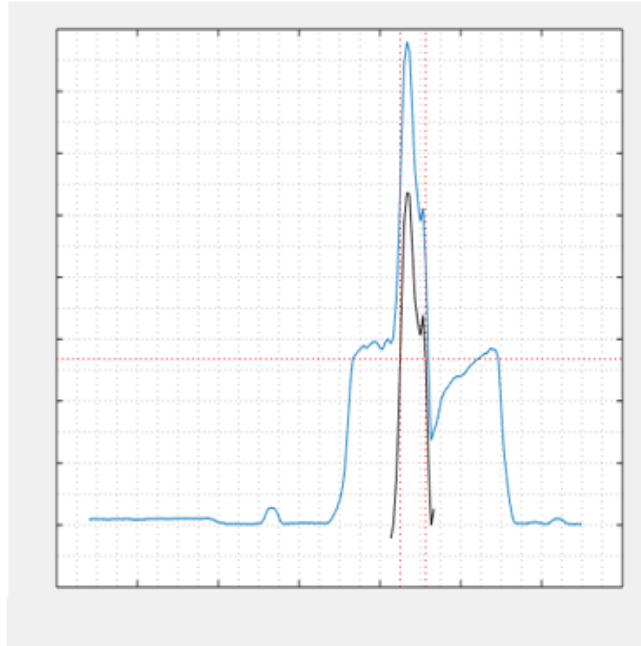




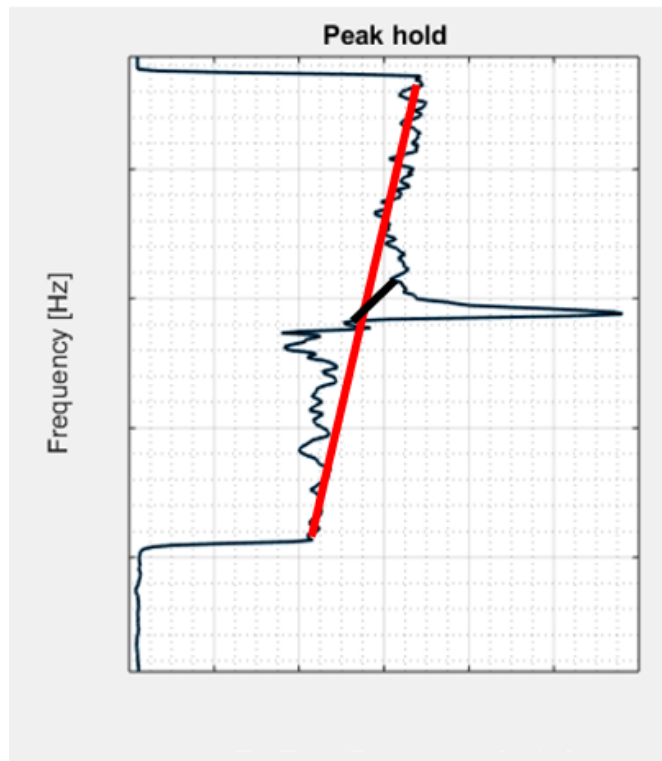
this point, and performs a linear de-trending causing the peak to partially go to negative amplitude, but keeping the peak shape intact, as shown in the following figure:



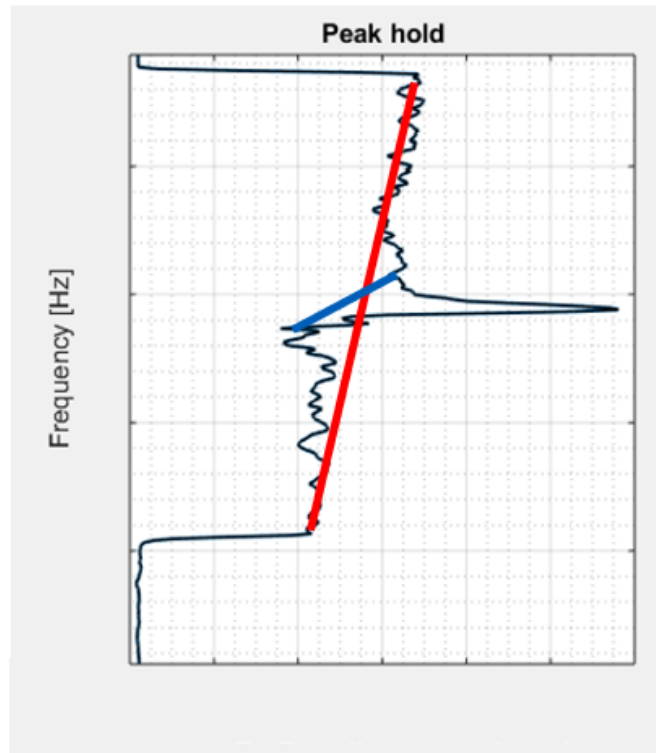
whereas considering the black line in figure 6.14, a de-trending based on the peak delimiters is performed, causing a partial deformation of the peak shape and therefore a variation in the Q factor estimation:



In this case, the relevant difference between the two approaches is mainly in the Q factor value, which is greater following the first de-trending method of the 32% , whereas the variation in amplitude is around the 6%. But obviously, these percentages are highly dependant on the angle formed by the two lines representing the different de-trending methods, for example, in this case:



the angle between the two de-trending methods is low, and therefore both the Q factor and amplitude difference is below the 2%, but a different result could have been obtained acting the peak de-trending following the blue line in the following figure:



resulting in a variation in terms of Q factor that is around 20% and an amplitude shift of the 6 %.

Therefore, as shown, the post-processing of the strain gauges acquisition system is highly variable and dependant on the user's choices, making it hard to automatize the method. Even a minimal difference in terms of peak delimiter estimation within the same de-trending method can cause a significant difference in terms of the results obtained, and furthermore, the number of strain gauges reliable was around the 40 % of the total, giving no room for a solid mean calculation. As we will see, the punctual data acquired by a specific SG compared with another acquisition method will be evaluated as coherent, but the ultimate decision was to exploit other sensors to validate the technology of interest, a set of gauges completely independent from magnetic disturbance.

### 6.3 The Blade Tip-Timing Measurement System

BTT systems work on complex processing systems developed for the first time more than 30 years ago from researchers of the Arnold Air Force Base, NASA and Brown Boveri [13] [1] employing a set of non-contact sensors mounted on the casing and facing the blades of a rotating bladed disk [22] [20] [12].

This innovative method is introduced in substitution of the strain gauges measurement systems. As a matter of fact, the latter is an intrusive method, which can, therefore, modify the dynamic or fluid-dynamic of the phenomenon, and which requires a complex telemetry system to transmit data. Furthermore, the BTT allows acquiring data from all the blades together at the same time, whereas the strain gauges system acquires data just from the blades where the gauge is applied.

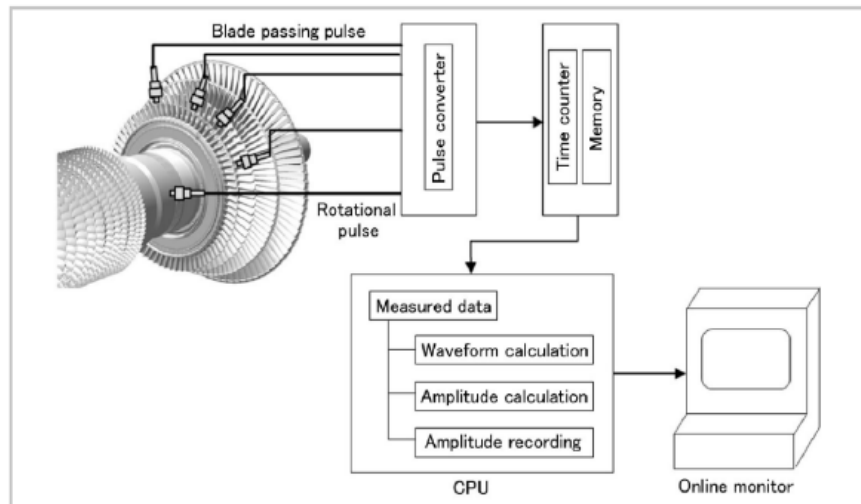


Figure 6.15: BTT measurement system [18]

The physical concept behind this acquisition system is relatively simple; it is in fact based on the comparison between the predicted ToA (Time of Arrival) of a specific blade in front of a stationary sensor, which depends just on the rotational speed of the disk compared with the effective ToA, which is a function of blade vibration. This means that blades vibration can be connected with time variation.

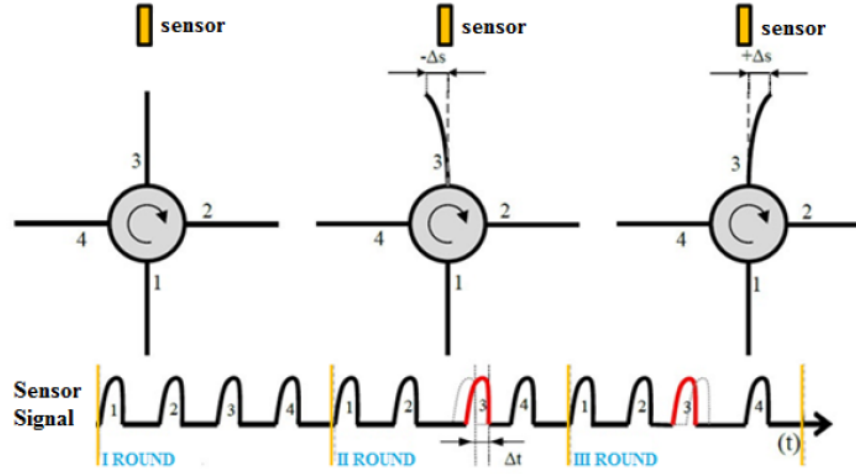


Figure 6.16: ToA variation [18]

In figure 6.16 a practical example is given. Here we have a disk with four blades, which rotates in front of a fixed sensor. Considering Round I, here all the blades stand firm, do not causing any phase shift. By contrast, in the other two rounds, a time-shift  $\Delta t$  is caused by the tip vibration of blade 3, and this information can be easily related to the vibration of that specific blade by knowing its rotational velocity and the radius of the blade. Obviously, the more the data acquired, the better, and very complex results can be obtained by using BTT, as will be explained later in this chapter.

After a brief introduction to the method exploited, from now a description of the equipment used in the Test Rig aforementioned is given.

The BTT adopted in the test of reference is a latest generation system that uses optical laser sensors. For the dummy disks 1 and 2 all the tests were performed by employing five sensors for the direct detection of the blades ToA and an additional sensor ( $1/rev$  sensor) measuring the rotational speed and representing the reference for all the others. The signal from the  $1/rev$  sensor was acquired by both the BTT and the strain gauges system in order to synchronize the measured blade vibrations signals during the post-processing operations.

### 6.3.1 The Beam Shutter Method and the Sensor Positioning

The standard measurement approach for the BTT method is based on a set of sensors that are positioned along the radial direction in order to detect the ToA at the blade tip where the maximum vibration amplitude occurs. Although this sensor positioning

is particularly suitable for a disk with tip-free blades, it is impracticable for shrouded bladed disks. In fact, due to the presence of shrouds, the laser sensors wouldn't have been able to capture the motion at the tips. For this reason, a new sensor configuration called *beam shutter* was tested and their position is shown in figure 6.17 and 6.18:

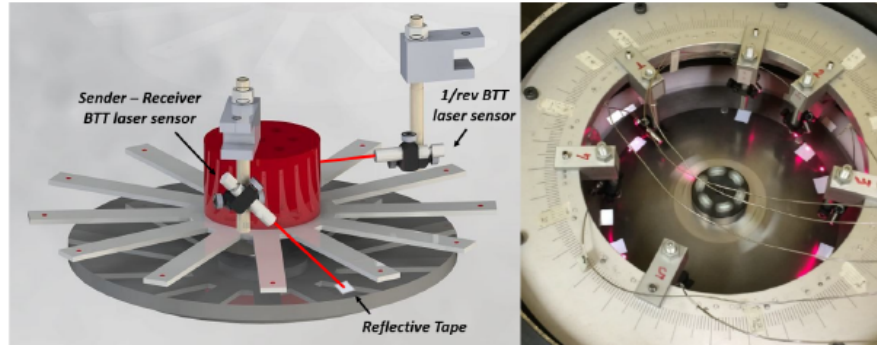


Figure 6.17: Beam shutter configuration for the dummy disk 1 [3]

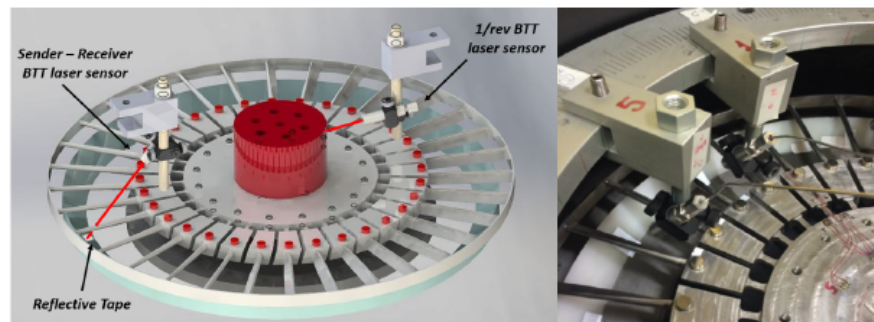


Figure 6.18: Beam shutter configuration for the dummy disk 2 [3]

While the application of figure 6.17 tested the capabilities of the beam shutter configuration when the OOP vibration modes of the blades have to be detected, the case of figure 6.18 clearly shows the need for measuring the vibrations at the blade trailing and leading edges since a direct detection of the vibrations at the blade tips cannot take place.

For both the applications, each sensor was mounted above the disk and produced a laser beam that was collimated through a lens on a reflective tap stuck on a fixed surface beneath the disk, in order to overcome the problems connected with the *beam interrupt* method presented in [21]. During the disk rotation, the passing blade acts as a shutter, blocking the returning light towards the sender-receiver sensor. The system was set up in order to direct the laser beam towards the leading and trailing edge locations where the blade experienced the maximum vibration amplitudes. The optical sensors and the

reflective tape were employed in measurements performed without any significant temperature variation from the room temperature.

The sensors were installed at the same distance from the disk centre, and their relative circumferential position was chosen in both the cases by means of an optimization tool, which avoids the aliasing effect in the identification of the travelling wave mode shape characterizing the vibrating disk. The optimization tool requires as input the number of sensors the expected engine orders and the number of blades.

## 6.4 BTT Postprocessing

As aforementioned, there are several advantages connected with this acquisition method in an application as the one described up to this point:

- By definition, it is immune to magnetic disturbance
- It is a non-intrusive measurement system
- Data are acquired for each blade, not just the ones where the sensors are installed, allowing to evaluate the blade-to-blade variation.

An ad-hoc tool was used to perform the post-processing, and from now, a brief description of its working method is given. First of all, the angular position of the sensors is identified, and it is possible to customize blades numeration in order to be consistent with the strain gauges case.

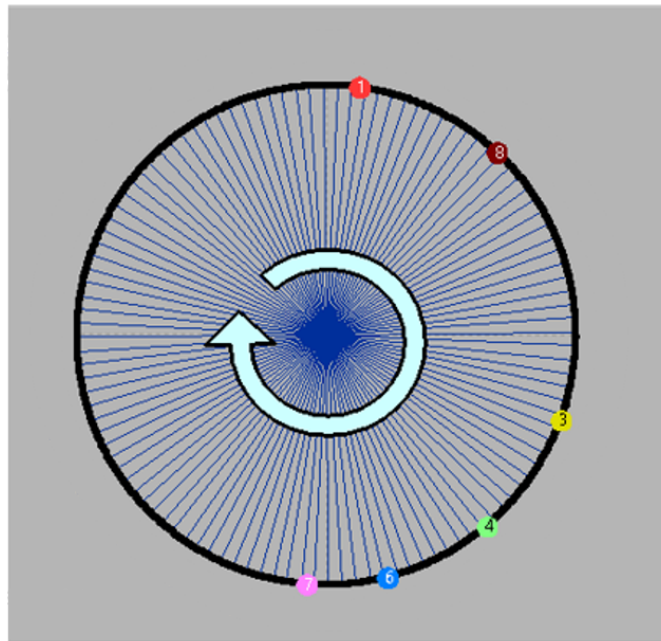


**Figure 6.19: Angular sensors' position**

then, the velocity profile is acquired, thanks to a  $1/rev$  sensor as previously explained as shown in figure 6.20

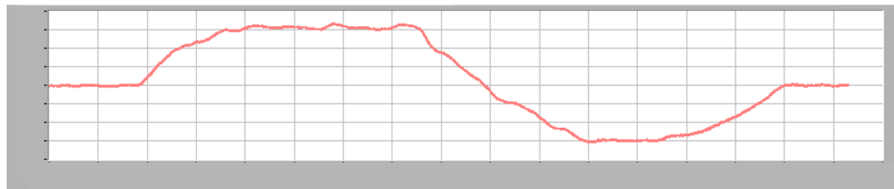


**Figure 6.20: Velocity profile**

and from this profile, a ramp is selected in order to have a sweep in frequency to analyze. The following step is performed to understand the quality of the data acquired from each sensor, it is based on the Inter-blade distance acquired by the gauges, and if one of them shows an incoherent evaluation of the blade-to-blade variation, it has to be considered inaccurate, and it is therefore excluded from the analysis.

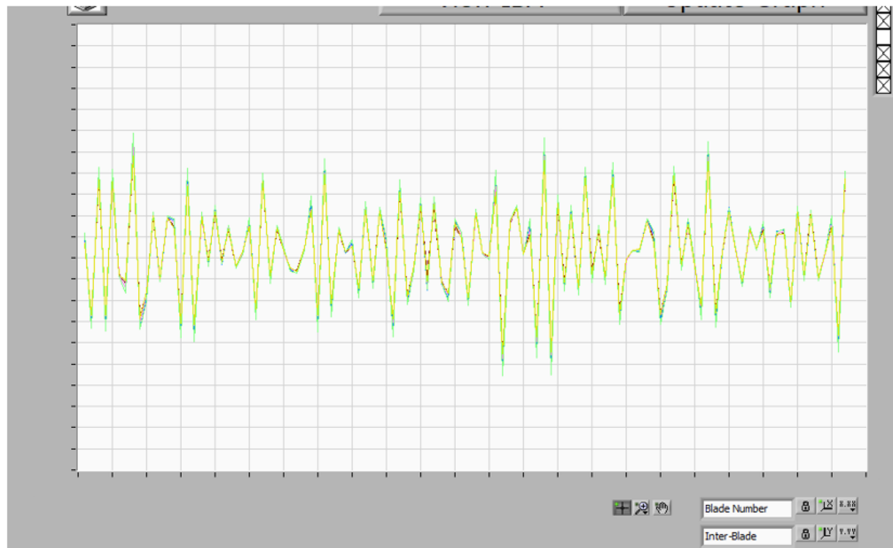


**Figure 6.21: Inter-Blade Distance evaluation**

After having set all the frequency analysis parameters, it is then possible to obtain the FFT result obtained by all the different sensors:

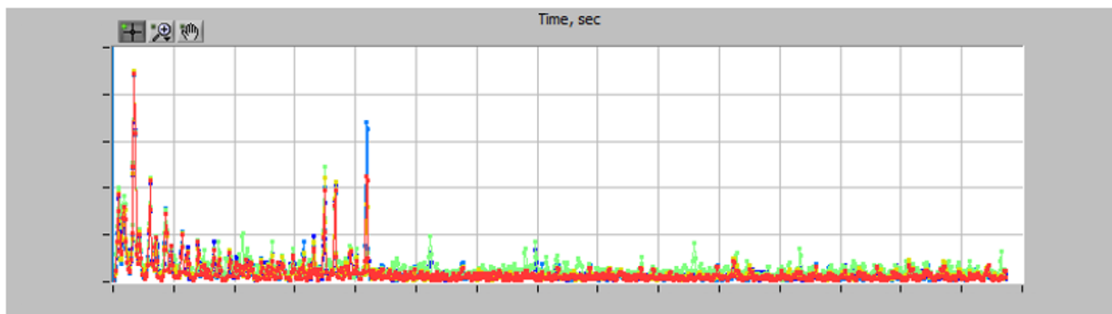


**Figure 6.22: FFT result**

and the peak shape for each blade is then obtained, allowing to evaluate both Q factor and vibration amplitude:

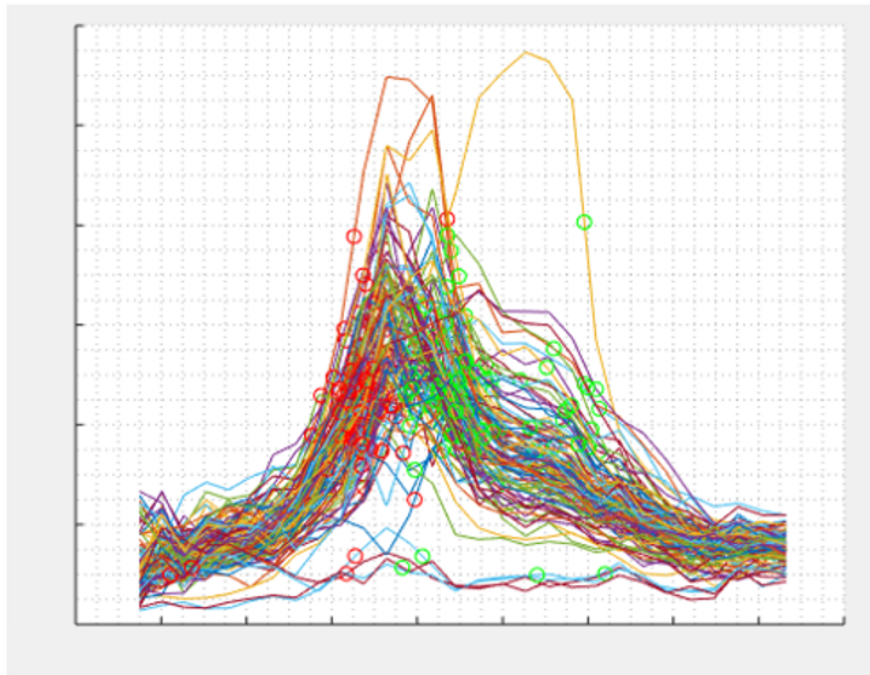


Figure 6.23: Peak shape evaluation for each vibrating blade

Therefore compared to the strain gauge acquisition method, some advantages can be easily identified:

- In this case, we have 100% of the acquisition channels available, compared to the 40% of the traditional measurement system
- It doesn't suffer from any magnetic disturbance
- As a consequence, there is no need for a user conditioned de-trending
- The output is given for each blade, whereas the strain gauges acquire data just on the blades where they are installed, which means that the mean value is highly reliable.

The intention now is to make a comparison between the two acquisition systems' output, in order to further investigate what has been described up to this point.

Let's consider the BTT output of Blade 52 where is installed the SG04, which corresponds to a high-quality code for the Strain gauges acquisition. The result in terms of frequency spectrum for the SG04 is showed in figure 6.24

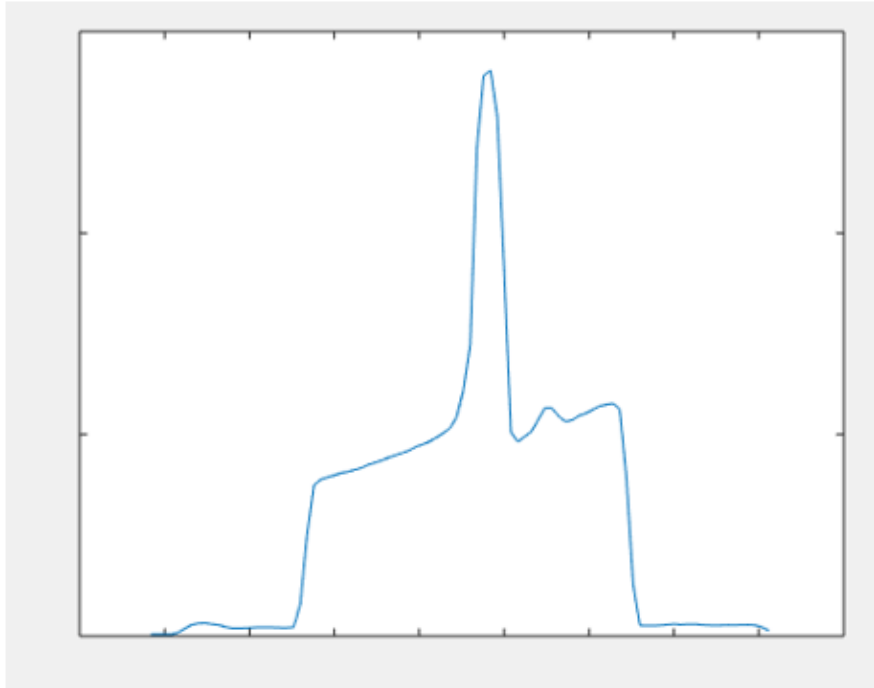


**Figure 6.24: SG04 frequency spectrum**

whereas in figure 6.25, the output of the tip timing analysis on blade 52 is showed:

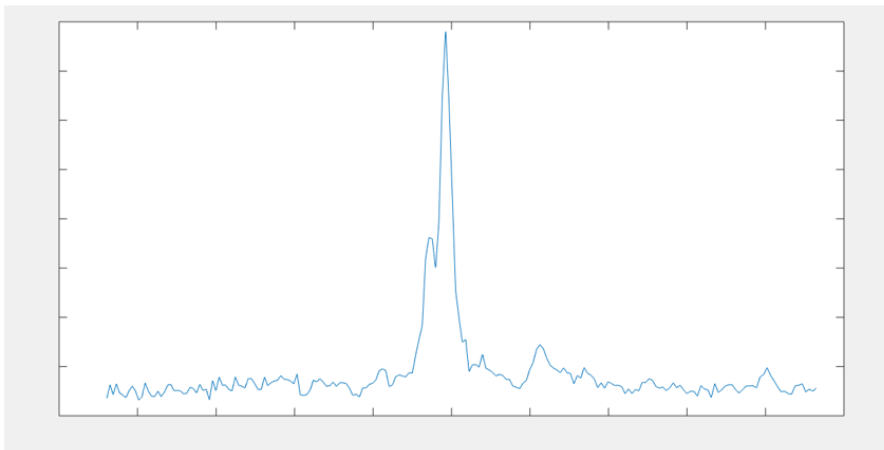


**Figure 6.25: Blade 52 frequency spectrum**

by overlapping the two results, the following figure is obtained:

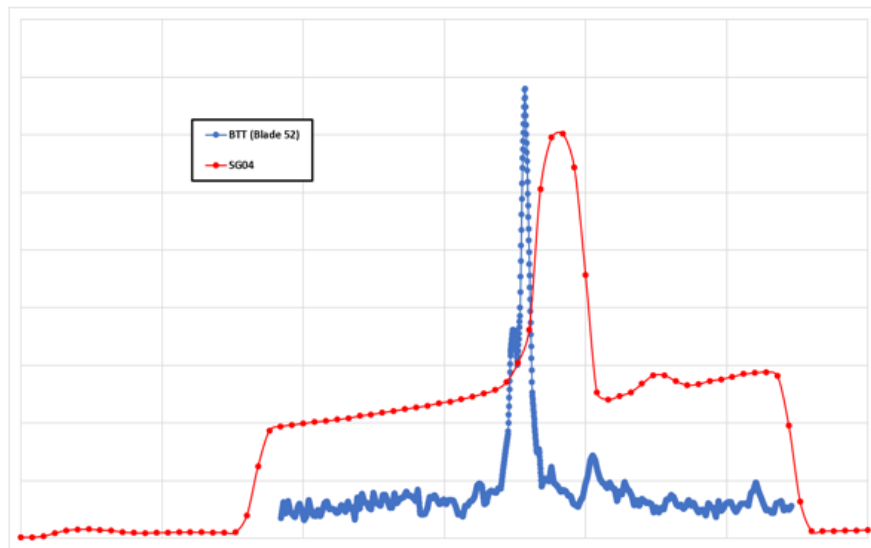


**Figure 6.26: SG04 vs Blade 52 frequency spectrum**

Analysing more in depth figure 6.26, some considerations can be made:

- A frequency shift is identified, even if it is below the 5% variation, probably due to a difference between the frequency analysis parameters chosen. In fact, the two signals to be analyzed were different, requiring a distinct windowing period, which could have caused a different energy discretization
- Amplitude variation is around the 15%, whereas the Q factor delta is 60%
- The red curve shows a linear offset caused by the magnetic disturbance to whom strain gauges are subjected
- It is important to notice that if the de-trending process would have been applied, the amplitude variation would substantially increase, up to the 45%

By comparing the two acquisition methods for different test points, the following plot is obtained:

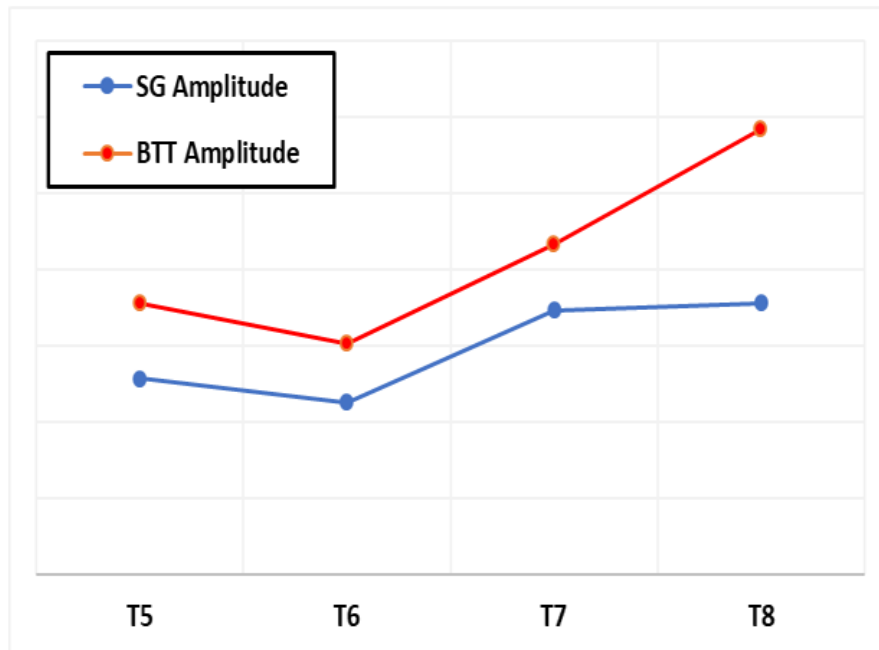


Figure 6.27: SG method vs BTT

where the x-axis increases with the magnetic forcing, and on the ordinates there is vibration amplitude.

Some considerations can be made:

- As we can see a similar trend is obtained, thanks to the accurate selection of data performed on SGs output, which means that the problems were partially overcome
- An amplitude offset is identified, probably due to an aleatory de-trending process, and the occurrence of cases as shown in figure 6.26 where the composition of noise and the effective signal is more complex than a linear sum.
- The highest difference is spotted at high rotational speed, which corresponds to the greatest magnetic disturbance, and again the result is conditioned by a non-objective de-trending.

## Chapter 7

# Conclusions

During this thesis work, a postprocessing tool was improved and specialized for being applied to a non-conventional vibrational test to analyze a new technology of interest. The code written in MATLAB was meant to substitute an existing black-box software employed for the frequency analysis of raw data and which guarantees the integration with a dashboard. The development of an in-house code allows to further customize the analysis parameters, besides decreasing the computational time of the 80%. A benchmarking activity was followed in order to validate the code output, and a GUI (Graphic User Interface) was developed, to make the entire code more user friendly.

The postprocessing activity involved two main acquisition methods: Strain Gauges (SG) and Blade Tip Timing (BTT). The former was the traditional method, which appeared to be highly affected by magnetic disturbance, causing the data to be subjected to a high noise to peak ratio. Therefore an ad-hoc functions set was coded to overcome these problems when possible, and exclusion of data based on signal quality is performed, in order both to base the postprocessing on reliable data and to identify the optimal testing conditions. The results showed a non-objective behaviour, which is mainly affected by different detrending solutions that the user can follow.

A more innovative acquisition method is therefore considered, which is independent by any magnetic disturbance, the laser-based Blade Tip Timing method. A dedicated tool is used to post-process the sensors' data which has been briefly introduced both in terms of input required and output obtained. The amplitude and Q factor estimation follows, and a punctual comparison between the two acquisition methods is suggested, which clearly shows a coherent trend by following both the approaches, but also substantial differences related to a user conditioned postprocessing. Therefore, taking all these factors into account, the optimal solution for the validation of the technology analyzed is identified in postprocessing the data with the BTT method.

# Bibliography

- [1] NASA TM-81382. «Digital system for dynamic turbine engine blade displacement measurements». In:
- [2] S. Gade et al. *Order Tracking Analysis*. Tech. rep. Brüel & Kjaer, 1995.
- [3] Giuseppe Battiato. «Vibrations Prediction and Measurement of Multi-Stage Bladed Disks with non Linear Behavior due to Friction Contacts». PhD thesis. Politecnico di Torino, 2017.
- [4] Fabio Belacicco. «Stabilizzazione di uno stadio di LPT bladed-disk in presenza della condizione di instabilità a flutter mediante mistuning intenzionale». MA thesis. Politecnico di Torino, 2016.
- [5] Teresa Maria Berruti, Vanni Maschio, and Paolo Calza. «Experimental Investigation on the Forced Response of a Dummy Counter Rotating Turbine Stage With Friction Damping». In: vol. 134. June 2012. DOI: 10.1115/GT2012-69059.
- [6] Eleonora Caponio. «Calcolo della risposta forzata di componenti per motori aeronautici in presenza di contatti per attrito». MA thesis. Politecnico di Torino, 2018.
- [7] Lorenzo Capra. «Methods for the analysis of aeronautical gearbox experimental data». MA thesis. Politecnico di Torino, 2019.
- [8] Matthew P. Castanier and Christophe Pierre. «Modeling and Analysis of Mistuned Bladed Disk Vibration: Current Status and Emerging Directions». In: *Journal of Propulsion and Power* 22.2 (2006), pp. 384–396. DOI: 10.2514/1.16345. eprint: <https://doi.org/10.2514/1.16345>. URL: <https://doi.org/10.2514/1.16345>.
- [9] Audrey F. Harvey and Michael Cerna. «The Fundamentals of FFT-Based Signal Analysis and Measurement in LabVIEW and LabWindows». In: 1993.
- [10] Marco Lassalle. «Self-excited vibrations controlled by damping at blade root joints of turbine disks». PhD thesis. Politecnico di Torino, 2018.
- [11] Francesco Giovanni Lauria. «Automatic tool development for LPT preliminary assessments». MA thesis. Politecnico di Torino, 2019.

- [12] M.Zielinski and G.Ziller. «Noncontact Blade Vibration Measurement System for Aero Engine Application». In: 2005.
- [13] Peter Eugene McCarty and J W Thompsonk. «Development of a Noninterference Technique for Measurement of Turbine Engine Compressor Blade Stress». In: 1980.
- [14] Letizia Lo Presti. *L'analisi dei segnali*. Ed. by Clut. 1992.
- [15] Davide Prino. «Automatic Preliminary Assessment of the mechanical response of LPT stages». MA thesis. Politecnico di Torino, 2018.
- [16] Amedeo Ramieri. «Analisi e comparazione di diversi modelli di contatto all'interlocking per rotori di turbine di bassa pressione». MA thesis. Politecnico di Torino, 2017.
- [17] *Strain gauge*. [https://en.wikipedia.org/wiki/Strain\\_gauge](https://en.wikipedia.org/wiki/Strain_gauge).
- [18] Roberto Tomassini. «Blade Tip Timing and Blade Tip Clearance Measurement System Based on Magnetoresistive Sensors». PhD thesis. Università degli Studi di Padova.
- [19] *Triangolo di Collar*. <https://aerospaceengineeringblog.com>.
- [20] Y.I Zablotskij and Y.A. Korostelev. «Measurement of resonance vibrations of turbine blades with the elura device.» In: *Energomashinostroneniye (USSR)* 2 (), pp. 36–39.
- [21] M. Zielinski. «Vibration Measurements on Compressor Blades and Shrouded Turbine Blades». In: *14 Blade Mechanics Seminar* (2009).
- [22] M Zielinski and G Ziller. «Noncontact vibration measurements on compressor rotor blades». In: *Measurement Science and Technology* 11 (June 2000), p. 847. DOI: 10.1088/0957-0233/11/7/301.

